國立交通大學

加速器光源科技與應用碩士學位學程

碩 士 論 文

利用同步輻射紅外光分析 Fe_3O_4 和 $Fe_3O_4@SiO_2$ 奈米材料對人類肺腺癌活細胞的影響

Synchrotron Radiation Infrared Ray Analysis of Human Lung Adenocarcinoma Living Cells Upon Exposure to Fe_3O_4 and $Fe_3O_4@SiO_2$ Nanomaterials

研 究 生：陸意德

指導教授：吳樸偉 教授

賴麗珍 博士

中華民國 一百零一 年 七 月

利用同步輻射紅外光分析 Fe_3O_4 和 $Fe_3O_4@SiO_2$ 奈米材料對人類肺腺癌活細胞的影響

Synchrotron Radiation Infrared Ray Analysis of Human Lung Adenocarcinoma Living Cells Upon Exposure to Fe_3O_4 and $Fe_3O_4@SiO_2$ Nanomaterials

研 究 生：陸意德　　Student: I-Te Lu

指導教授：吳樸偉　教授　　Advisor: Prof. Pu-Wei Wu

賴麗珍　博士　　Dr. Lee-Jene Lai

國 立 交 通 大 學

加速器光源科技與應用碩士學位學程

碩 士 論 文

A Thesis

Submitted to Graduate Program for Science and Technology of Accelerator Light Source

College of Engineering

National Chiao Tung University

in Partial Fulfillment of the Requirements

for the Degree of

Master

in

Graduate Program for Science and Technology of Accelerator Light Source

July 2012

Hsinchu, Taiwan, Republic of China

中 華 民 國 一百零一 年 七 月

利用同步輻射紅外光分析 Fe_3O_4 和 $Fe_3O_4@SiO_2$ 奈米材料對人類肺腺癌活細胞的影響

學生：陸意德　　指導教授：吳樸偉 教授

賴麗珍 博士

國立交通大學加速器光源科技與應用碩士學位學程

摘要

氧化鐵磁性奈米粒子(Fe_3O_4 MNPs)以及二氧化矽包覆氧化鐵磁性奈米粒子($Fe_3O_4@SiO_2$ MNPs)在生醫方面漸漸變成很重要的應用，然而這種磁性奈米粒子對於細胞的影響仍然不是很清楚。因為表面修飾的氧化鐵磁性奈米粒子以及二氧化矽包覆氧化鐵磁性奈米粒子，其表面修飾物可能會在進入細胞時或是在細胞內被移除而形成裸露的氧化鐵磁性奈米粒子，因此裸露的氧化鐵磁性奈米粒子以及二氧化矽包覆氧化鐵磁性奈米粒子應該需要受到注意。在這個研究中，為了避免太多的前驅物殘留在奈米粒子上，氧化鐵磁性奈米粒子採用共沉降法來合成，而二氧化矽包覆氧化鐵磁性奈米粒子則利用 Stöber 法合成。藉由 X 光繞射儀(XRD)、穿透式電子顯微鏡(TEM)、X 光光電子能譜儀(XPS)、X 光吸收光譜(XAS)以及超導量子干涉磁量儀(SQUID)來量測這些磁性奈米粒子的性質以及特性，結果顯示合成的氧化鐵奈米粒子是以四氧化三鐵的相為主，而二氧化矽則是以非晶態沉積在氧化鐵奈米粒子上，這些合成的磁性奈米粒子都具有超順磁的特性。A549 肺腺癌細胞被用來做為這些磁性奈米粒子處理的模式細胞，其細胞活性藉由 MTT 法檢測來取得。結果顯示經過磁性奈米粒子處理的 A549 細胞呈現出較低的粒線體還原酶活性。此外，同步輻射紅外光(SRIR)光譜以及同步輻射紅外光

顯微鏡(SRIRM, 擁有 10um 空間解析度)用來量測細胞內部的化學物質含量變化以及分布。結果顯示細胞內部的 DNA 結構間接地受到磁性奈米粒子的影響，其含量隨著磁性粒子的濃度增大以及作用時間而下降，雖然蛋白質以及磷脂質的結構沒有受到太大的影響，但它們的相對成分比例會隨著磁性奈米粒子作用的時間以及濃度，而有所不同;同時也可以觀察到暴露在磁性奈米粒子中 A549 細胞以及對造組 A549 細胞中，相對較多的蛋白質集中在核心，遠離核心的區域，磷脂質相對地比較多量。

Synchrotron Radiation Infrared Ray Analysis of Human Lung Adenocarcinoma Living Cells Upon Exposure to Fe_3O_4 and Fe_3O_4@SiO_2 Nanomaterials

Student: I-Te Lu Advisor: Prof. Pu-Wei Wu

Dr. Lee-Jene Lai

Graduate Program for Science and Technology of Accelerator Light Source

National Chiao Tung University

Abstract

Fe_3O_4 and Fe_3O_4@SiO_2 magnetic nanoparticles (MNPs) have recently become important in biomedical applications; however, influences of these MNPs to cells are still not very clear. Bare Fe_3O_4 and Fe_3O_4@SiO_2 MNPs should be noticed because any surface modification may be removed from them when they enter into cells or in cells. In this work, in order to avoid too much surface residues from the precursors, coprecipitation method is adopted to synthesize bare Fe_3O_4 MNPs, while Stöber process is performed to synthesize bare Fe_3O_4@SiO_2 MNPs. The characterization of MNPs is indentified by X-ray Diffraction (XRD), Transmission Electron Microscopy (TEM), X-ray Photoelectron Spectroscopy (XPS), X-ray Absorption Spectroscopy (XAS) and Superconducting Quantum Interference Device Magnetometer (SQUID).

These results show that as-prepared Fe_3O_4 MNPs primarily contains crystalline Fe_3O_4 phase, while the deposited SiO_2 on Fe_3O_4 MNPs is amorphous. A549 lung cancer cells are used as model cells for MNPs treatment, and the cell viability is measured by 3-(4,5-dimethylthiazol-2-yl)-2,5-diphenyltetrazolium bromide (MTT) assay. The results show that mitochondrial reductase activity in cells is reduced by treating Fe_3O_4 MNPs and Fe_3O_4@SiO_2 MNPs to A549 cells for 36 hr. Instead of traditional biochemical methods, synchrotron radiation infrared-ray (SRIR) spectra and synchrotron radiation infrared-ray microscopy (SRIRM) with high spatial resolution 10 μm are carried out to measure the change of chemical components and chemical composition distribution in cells. These results exhibit that DNA structures in cells are indirectly affected by Fe_3O_4 MNPs and Fe_3O_4@SiO_2 MNPs, and the concentration of DNA becomes less with MNPs concentration and treatment time while no protein and lipid changes are observed, but the lipid/protein ratio is MNPs-concentration-dependent and treatment-time-dependent and it is observed that the amount of lipids is relatively larger at far-nucleus regions while that of proteins is relative larger at and around the nucleus region.

Acknowledgement

首先，很感謝兩位指導老師－吳樸偉老師以及賴麗珍老師，這兩年來在研究上的指導與鼓勵。也很感謝擔任口委的陳三元老師與劉典謨老師，在口試時給予許多寶貴的建議，引導我更多的思考方向。

吳樸偉老師是我學習邏輯思考的典範，常常要求以及訓練我們學生要有邏輯思考的能力，我也發現許多經過博士班訓練的老師們，這方面的能力都很強，這是我在吳老師身上學習到的第一點。第二點是，吳樸偉老師對於經過仔細思考所得的結論會非常堅持，雖然這樣的堅持一開始可能看不出成果，不過往往事實證明老師的堅持是對的，這讓我學習到仔細地判斷方向是一個領導人所需具備的。並且，經過思考後或是有新的證據出現時，導出新的結論，會勇於修正自己之前的結論。這樣的科學研究精神，也使我獲益良多。第三點是吳老師常常會分享許多人生經驗以及故事，勉勵學生要有遠大的志向以及認真努力的做事精神，然後自己會做榜樣，跟我們一起學習。

同時，也很感謝賴麗珍老師，賴老師是我學習做實驗的榜樣，每當使用新的光束線出問題時，老師就會當場思考出現問題的地方，然後 input 一下，再看一下 output，漸漸地問題就開始 narrow down 到某幾個地方，針對這些地方做修正，這樣的研究方式豐富了做實驗的學習經驗。此外，每當我實驗做錯，老師會馬上跟我討論，然後立刻請我重做，雖然很累，但是這種當下修正錯誤讓我學習到「錯誤沒有關係，但要從中學習經驗」。老師也常常教我們數據分析的方式以及某些軟體的使用方法，初步的教導後，剩下的就交給我們自己去摸索了。我很喜歡這樣初步帶一下之後，放手讓我學習的感覺。希望之後，可以訓練出獨當一面，能夠從無到有的學習能力。

接著，要感謝的是我的家人。很感恩爸爸媽媽還有弟弟，常常會有事沒事的，

打電話給我，關心一下我的近況。並且辛苦地工作，讓我無後顧之憂地完成碩士學位。也很感謝我的女朋友王婷儀，自從我大三進入實驗室之後，幾乎每個週末來新竹，許多時間都是在實驗室渡過，讓我可以專心讀書做實驗以及準備各式各樣的考試。然後會很細心地幫我處理許多非學業的瑣碎事情，我很感謝她。

此外，也很感謝許多研究路上的師長與夥伴。感謝我量子力學以及電動力學的老師，陳永富教授，我經常找他聊聊讀物理遇到的問題，他會很有耐心地教導以及分享他的一些事情以及建議。也要感謝劉典謨教授，向我分享有趣的新聞以及文章，讓我打開科學知識的視野。也很感恩謝育淇學長，平常會跟我討論有關科學的知識以及夢想，他對實驗的熱情影響了我許多。我從他們身上漸漸地發現自己對於科學研究的熱情。我還記得諾貝爾生理學家 David Baltimore 說的話：「我把生命奉獻於人類智識的增加，我們無須為科學研究另添冠冕堂皇的理由。」這樣的熱情，我很開心，我發現到了。

感恩學校實驗室的大學姊陳境妤，對於實驗室的維護，以及非常有秩序的建立實驗室的點點滴滴，讓我們有很好的研究環境。感恩同步的研究助理謝嘉濬，很多次幫助我完成實驗。每當操作光束線，熬夜了許久，我沒有體力的時候，幫助我繼續完成剩下的部分，以及新報到的研究助理林思妤學姊，也很感謝她的協助。此外，很謝謝這屆碩二的同學，許議文、郭哲瑋、邱尊偉、李孟翰以及董正霖，跟我奮鬥了兩年，彼此互相幫忙以及學習，熬夜趕報告做報告，還有許多次幫我買便當。感謝同步學姊謝怡慧以及學長朱鴻霖，平常在同步做實驗的建議，以及快樂的相處時光。還有感謝賴俊翰學長以及蔡和成學長，分享許多準備留學的經驗，讓我體會在國外可能會遇到的強者的學習態度，因此積極學習，期望可以跟這些強者們一起討論科學的知識以及能夠跟得上他們的腳步。也很感恩張雲閔學長，留在實驗室很晚，守護著實驗室，希望大家都能夠平安無事，往往是最後一個離開。謝謝黃苡睿學長，在我進入實驗室後，教導我做實驗的方式。謝謝

張玉塵、謝逸凡以及林勝結學長，平常生活上的照顧，也謝謝陳致源、張詠策、張立忠、李佳勳學長們以及邱于凡、王儷曄、陳儷尹學姊們，在我剛進入實驗室時的照顧。很謝謝跟我們相處一年的黃冠傑學長以及陳琪、陳婉瑩、周亮余和黃筱琳學姊們分享許多修課與做研究的方式，以及最後留下來念博班的廖晨宏學長，往往跟我們打成一片，幫助我們許多忙。還有感謝新進入實驗室的陳精華學姊，常常會到 facebook 給我鼓勵。還有謝謝短暫來實驗室當研究助理的蔡志芳學長，曾經跟我一起為公費考試而奮鬥，以及短暫讀博班的學長陳光澤一起生活的樂趣，還有回來讀博班的張庭瑜學姊，雖然很少遇見她，不過一起在星期一早上來實驗室享受讀書的樂趣。還有謝謝分享同步輻射光 TXM 時間的同學黃柏翰，讓我不用每次熬夜做實驗，然後一起奮鬥撐過熬夜的時段。還有感謝碩一同學們，陳欣儀、梁雁汝、林韋霖、李依睿、林建程、傅宥閔這一年許多瑣事的幫忙，說不完的感謝。也感謝這屆新進入的碩一同學們，孫佑、蔡延璋、丁宣維、葉晟瑋、陳詠民，幫忙口試場地以及準備。最後，感謝所有在 facebook 上給我建議以及祝福的朋友們，還有大學部學弟妹們，讓我可以準備物理冶金課程以及晶體繞射課程，這之間教學相長，讓我學習許多。還有謝謝一起研究的高中生林鵬以及所有幫助過我的人。也感謝系辦傅玲如姐姐這兩年的照顧。

我會繼續我的夢想.....

諾貝爾獎的研究實力，

企業家的行事效率以及影響力，

教育家的無私奉獻以及教導。

2012.08.03 陸意德 at NCTU

Contents

List of Tables

List of Figures

Chapter 1 Introduction

Nanomaterials have been an important application in industries because of their novel properties, such as superparamagnetic properties emerging with the size of magnetic particles below their critical single domain sizes[1], tunable electronic properties[2], optical properties[3], thermal properties[4], catalytic properties[5] and etc. These novel properties will likely lead to a lot of commercial products appearing in market. However, toxicity of nanomaterials should also be taken into consideration as there is a chance that these nanomaterials may be exposed to human health and environment. Therefore, studies are needed to ensure that whether nanomaterials have toxic effects on human health and environment. Before determining why or which nanomaterials are toxic, one should have to understand how toxicity of nanomaterials is defined in term of reactive oxygen species (ROS), oxidative stress and gene expression by recent works[6-10].

Toxicity of materials is mostly based on cell viability, which is based on the features of living cells or dead cells, for instance, metabolic activities or cellular membrane integrity. Cell viability can be measured by several methods such as permeability of cell membrane (e.g., LDH assay or NR uptake assay), metabolic activity (e.g., MTT) and etc. However, these methods only measure particular constituent changes in cells, and generally speaking, this is not called toxicity of materials, but the influence of materials to living cells. Therefore, toxicity of materials requires broader specific definition.

Toxicity of materials means that materials have impact on cells' functions

associated with programmed cell death (another name, apoptosis) or necrosis. Programmed cell death means that there are some pathways, discussed below, in cells inducing the cell to decompose its components, such as deoxyribonucleic acids (DNA), proteins, lipids, carbohydrates and etc. Caspases (a group of proteases with cystein residue site in their catalytic site) are activated at the early apoptosis and triggering most of cellular changes during the death process, for instance, detachment of the apoptotic cell from its neighbors, cleavage and inactivation of proteins or activation of caspase activated DNase (CAD, which is responsible for attacking DNA into fragments) and etc.

There are two primary pathways, death-receptor pathway (extrinsic pathway) and mitochondria pathway (intrinsic pathway). Michael O. Hengartner who worked in Cold Spring Harbor Laboratory has reviewed for the biochemistry of apoptosis as displayed in Fig 1.1[11]. Basically, in the death-receptor pathway (Fig. 1.1 (left)), there are outside triggers, death ligands, proteins binding to trans-membrane death receptors, which activate caspase-8 by proteolyzing procaspase-8 via adaptor proteins, FADD. Caspase-8 is an initiator caspase that activates procaspase-3 into caspase-3, which is a member of effector caspases (caspase-3, -6, and -7) executing proteolysis in cells. In the other pathway, mitochondria pathway (Fig. 1.1(right)), caspase-9, another initiator caspase, is activated through the combination with Apaf-1 and cytochrome c to form apoptosome (active caspase-9). Both of Apaf-1 and cytochrome c are mostly contained in mitochondria when the mitochondria is intact, while the release of both into cytoplasm occurs when mitochondria is affected or disturbed, regulated by Bcl-2 family (e.g., Bax, Bid, Bcl-x_L, Bcl-2 and etc.), apoptotic regulators on the mitochondria membrane. Although these two pathways go through different

processes to activate initiator caspases, the final end step is triggering the same effector caspases (caspase-3, -6 and -7) (Fig. 1.1).

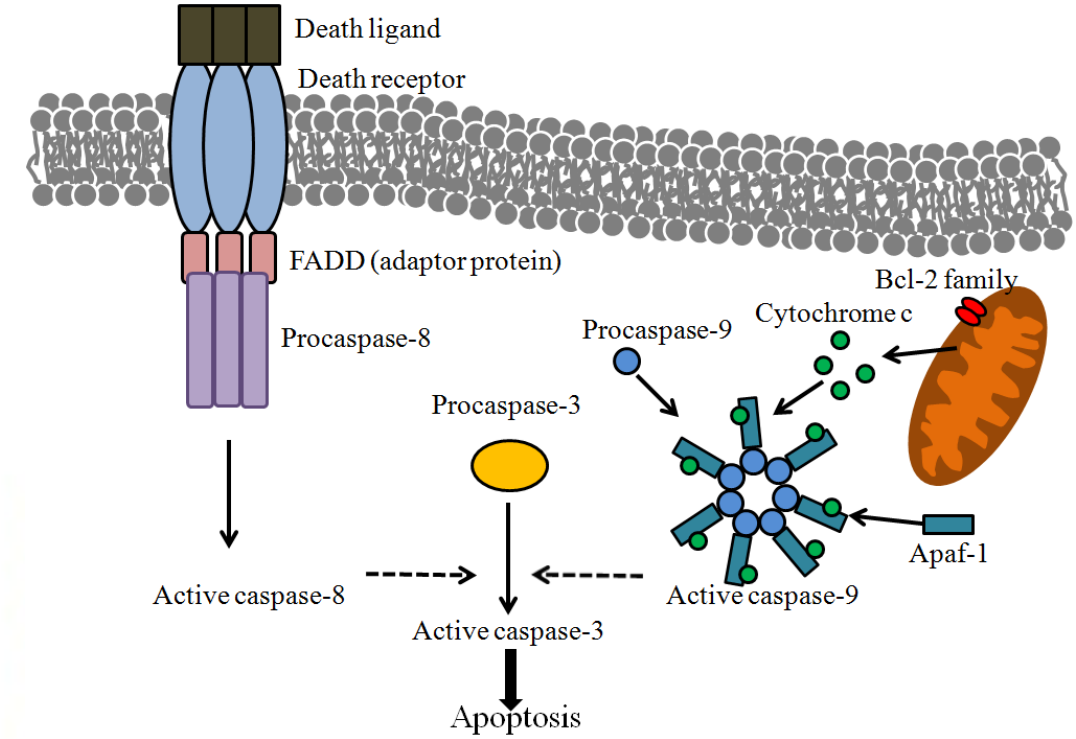

Figure 1.1 Apoptosis pathways: death-receptor pathway (left) and mitochondria pathway (right)[11].

The apoptosis pathways are obvious in some studies [9, 12], but the apoptosis being induced by the compositions of the materials or reaction mechanism of the materials is still not very clear. It has been observed that the amount of ROS arises when the nanomaterials interact with biological constituents in cells, causing lipid peroxidation, proinflammatory and cytotoxicity in the cells[10, 13-14]. This indicates that the production of ROS is related to toxicity in the biological sample. ROS has

oxidative capacity to oxidize biological constituents in cells, leading to the change of signal conduction pathways. Glutathione (GSH) in the biological sample is easily oxidized into glutathione disulfide (GSSG), causing the decline in the amount of GSH and the rise in the amount of GSSH. The ratio of the amount of GSH over GSSG is defined as oxidative stress, which means the ROS outweighs the antioxidant defense capacity of cells, causing redox disequilibrium in cells.

Different levels of oxidative stress could lead to different cellular responses, maybe protective or adverse to cells. There is a hierarchical oxidative stress hypothesis (three tiers)[15] describing the relationship of the relative level of oxidative stress and cellular responses (Fig. 1.2). For the first tier, the lowest level of oxidative stress, the cellular response involves the induction of protective antioxidant enzymes, regulated by the transcription and nuclear factor, erythroid 2-related factor 2 (Nrf-2 or NFE2L2) which induces the expression of various genes to produce several antioxidant and detoxification enzymes collectively called phase II enzymes including heme oxygenase 1(HO-1), NADPH quinine oxidoreductase (NQO1), superoxide dismutase, glutathione peroxidase and catalases. If the redox disequilibrium could not recover to normal condition by these antioxidant enzymes in the Tier 1, the further ROS production can activate proinflammatory responses such as cytokines and chemokines, mediated by MAP kinase and NF-κB cascades. For the highest level of oxidative stress, mitochondria membrane could be oxidized by ROS, lost its membrane potential and mitochondria may thereby open the permeability transport (PT) pore, releasing cytochrome c to induce apoptosis. Noteworthy is that nanoparticles may target mitochondria directly to disrupt the mitochondria membrane, thereby activating the apoptosis; however, the reason why nanoparticles directly target

mitochondria is unknown[16].

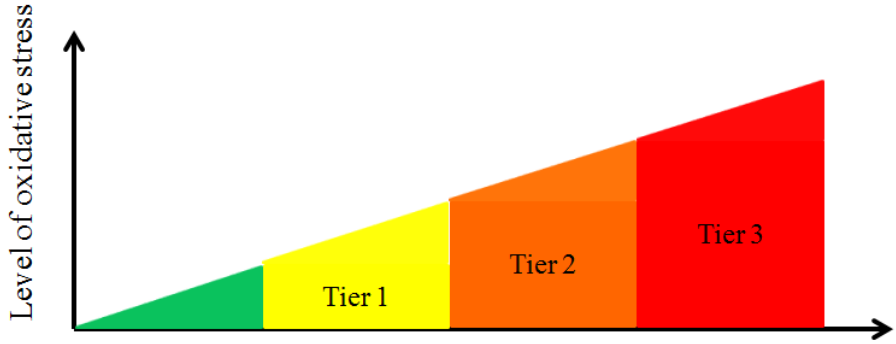

Cellular response	Normal	Antioxidant defense	Inflammation	Cytotoxicity
Signal pathway		Nrf-2	MAP Kinase NF-κB cascade	Mitochonrial permeability transition pore
Genetic expression		Anti-oxidant response element	AP-1 NF-κB	
Result		Phase II enzymes	Cytokines Chemokines	Apoptosis

Figure 1.2 The hierarchical oxidative stress hypothesis.

The hierarchical oxidative stress model provides a very clear relationship between oxidative stress and cellular responses. However, in order to understand a nanomaterial with a constant concentration which induces an oxidative stress level in cells, one have to conduct a lot of experiments; mostly, the amount of ROS production and the ratio of the amount of GSH/GSSG are measured with various concentrations, and which signal pathway the concentration of the nanomaterial induces should be investigated[8-9]. On the contrary, it cannot be denied that by these biochemical methods, one can specifically understand the mechanism of signal pathway the cells use upon exposure to nanomaterials.

One more thing, the other question about how nanomaterials generate ROS, which further destroys the redox equilibrium in cells, is still unclear. Although there are evidences that nanomaterials with proper electronic configurations that catalyze ROS generation can spontaneously produce ROS[17-18] with biological constituents in cells, nanomaterials without these properties still can generate ROS[6]. Therefore, ROS production may be not characteristic of certain materials, but the result of the interactions between biological systems and nanomaterials. How ROS are produced in this process still requires further investigation.

Fe_3O_4 and Fe_3O_4@SiO_2 MNPs become more and more important in biomedical fields, such as drug delivery[19-22], separation of biochemical products[20, 23] and biosensors[24-27]. Although these MNPs with proper surface modifications could exhibit no toxicity, there is a possibility that the surface modifications of these MNPs would be degraded in lysosomes in cells to expose their bare cores to biological systems. Thereby, the toxicity of bare MNPs should be examined.

The toxicity of Fe_3O_4 and Fe_3O_4@SiO_2 MNPs based on ROS has been recently studied by many researches [8, 28-33]. About the cytotoxicity of bare Fe_3O_4 MNPs, Karlsson et al.[30] has that no obvious toxicity, based on trypan blue, to A549 lung cancer cells at the particle concentrations (40 to 80 μg/ml) during 18 hr was observed, but they observed that, by comet assay, there was an increased DNA damage in A549 cells after 4 hr MNPs treatment time at the concentration 40 μg/ml. Könczöl et al.[8] also has demonstrated that no loss of cell viability was observed by the WTS assay and NR uptake assay when A549 cells were exposed to applied concentrations (10 to 200 $\mu g/cm^2$) after 24 hr MNPs treatment, during which they observed that ROS increased with MNPs concentrations. Although Fe_3O_4 MNPs do

not show cytotoxicty during 24 hr exposure time, there is a chance that Fe_3O_4 MNPs still remain in cells to influence cells function and cause cytotoxicity for more exposure time. Care must be taken when cytotoxicity of Fe_3O_4 MNPs is used to compare among different cell types, because various cells show different detoxification approaches[34].

With regard to SiO_2 nanoparticles, there was an evidence[10] that amorphous SiO_2 NPs showed a time- and concentration-dependent cell viability of A549 and cell viability of A549 reduced to 75 % at the applied concentration 50 μg/ml after 48 hr exposure, while 68% at 100 μg/ml at the same period of time. For different treatment time, when A549 cells were exposed to 100 μg/ml, cell viability further reduces from 68% after 48 hr exposure to 54.6% after 72 hr exposure. The author also showed that ROS increased and GSH declined with concentration and exposure time, suggesting an oxidative stress level increasing, which may explain the cell viability of A549 cell treated with SiO_2.

In this work, synchrotron radiation infrared-ray (SRIR) spectra are applied to study what biological constituents in cells are affected upon exposure to nanomaterials. Additionally, synchrotron radiation infrared-ray microscopy (SRIRM) with 10 μm spatial resolution is adopted to have the mapping of the biological components in the distribution of the cells, this high spatial resolution cannot be approached by other techniques. Besides, in this work, two nanomaterials Fe_3O_4 and Fe_3O_4@SiO_2 magnetic nanoparticles (MNPs) are used to demonstrate the SRIR spectrum change of A549 lung cancer cells with different MNPs concentrations and different MNPs treatment times.

Chapter 2 Background Information

2.1 Powder X-ray Diffraction (XRD)

The XRD technique, here, denotes wide angle XRD technique, not small angle XRD technique. What is wide angle XRD technique? The angle in this case is defined as the angle between the direction of incident beam and that one of the diffraction beam, called 2θ (Fig. 2.1). When this angle is larger than 5°, it is called wide angle; Contrast to small angle XRD technique, 2θ is approximate to 0°. Powder XRD technique is frequently used to determine the phase/phases appearing in a material.

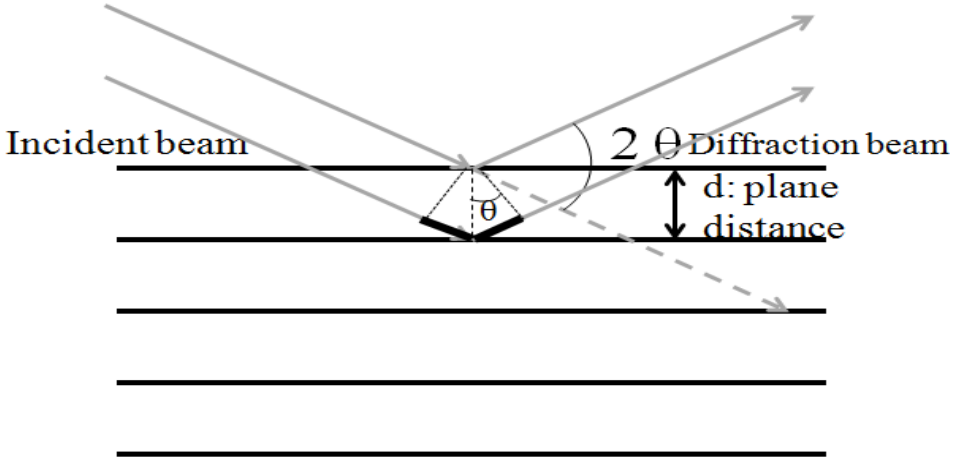

Figure 2.1 Scheme of Bragg's Law

When the incident light X-ray interacts with atoms in materials, X-ray will be scattered by these atoms. Scattered lights can be roughly categorized into two groups,

elastic scattering and inelastic scattering. Elastic scattering means no energy loss or change of the wavelength of the light after the light interacts with atoms, while inelastic scattering means the light loses energy and changes its wavelength after scattered by atoms. XRD belongs to elastic scattering, whereas the following discussed sections, XPS and XAS are inelastic scattering.

In powder X-ray diffraction technique, the powder of unknown material is illuminated by a constant wavelength, and this incident wavelength should be selected to avoid the absorption edge of the unknown material, that is, this photon energy should not be absorbed by the material. After atoms in the material scatter the X-ray, scattered X-ray forms constructive and destructive patterns in space and the intensity of these patterns are collected in the form of photons by a detector, which can be 2D imaging plate which can collect data within reasonable time or a point detector moving along a curve in space. For powders, the patterns are circular symmetric in space, so they are frequently expressed in one dimension as "Intensity versus 2θ", such as Figure 2.2. The XRD pattern is formed from construction and destruction of the scattered X-ray by atoms in a material, and thereby it reveals the information of the arrangement of atoms in the material and the composition of the material, because the positions of atoms can determine the diffraction pattern and the composition of the atoms provides the intensity of scattered X-ray.

In general, phase/phases in a material can be identified by the peaks appearing in the XRD pattern. The plane distance d (Fig. 2.1) can be determined by Bragg's Law, $2d\sin\theta = \lambda$, where θ is equal to $(2\theta)/2$, and λ is the wavelength of incident light. The crystal size D can be determined by Scherrer equation[35]:

$$D = \frac{K\lambda}{\beta \cos\theta}$$

where K is the shape factor (around 0.94 for spherical shape), λ is the incident wavelength, β is half the maximum intensity (FWHM) in radians and θ is the Bragg angle.

More quantitative phase analysis information contained in the XRD pattern can be obtained by Rietveld method.

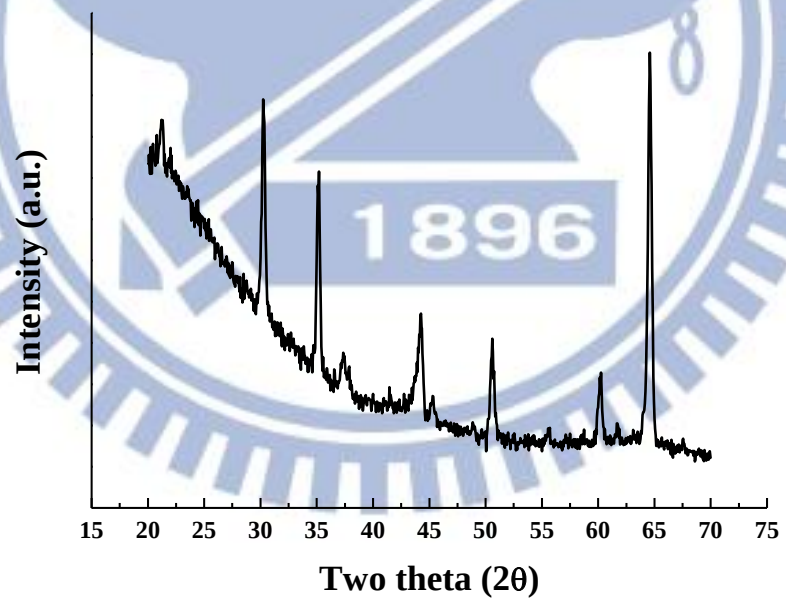

Figure 2.2 The XRD pattern of ITO substrate. The incident wavelength is 1.54Å .

2.2 X-ray Photoelectron Spectroscopy (XPS)

The incident X-ray with a constant energy, usually several hundred eV to keV, is used to bombard materials to knock out electrons in conduction bands, valence bands and core levels. These electrons carrying different energies are all collected by electron energy analyzer. The final result is expressed as "the number of electron accounts versus binding energy or kinetic energy" as shown in Figure 2.3. Since electrons in a specific element have their particular binding energies, XPS is therefore a chemical element analysis technique, and it is also called ESCA (Electron Spectroscopy for Chemical Analysis).

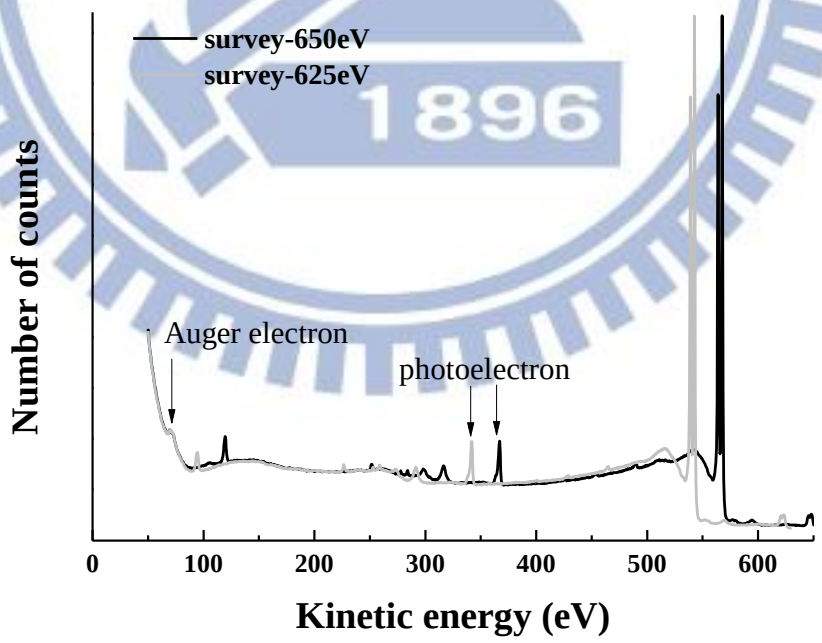

Figure 2.3 The XPS spectrum of a gold substrate.

Knocked-out electrons from a material can be photoelectrons or Auger electrons (Fig. 2.4). From Fig. 2.4, the kinetic energy of photoelectrons is not constant and determined by the energy of the incident X-ray, while the kinetic energy of Auger electrons is constant and dependent on the related energy levels. In order to distinguish them, incident X-ray with different energies should be carried out to irradiate this material. When two different photon energies are illuminating this material, photoelectrons show the same binding energy, while Auger electrons show the same kinetic energy.

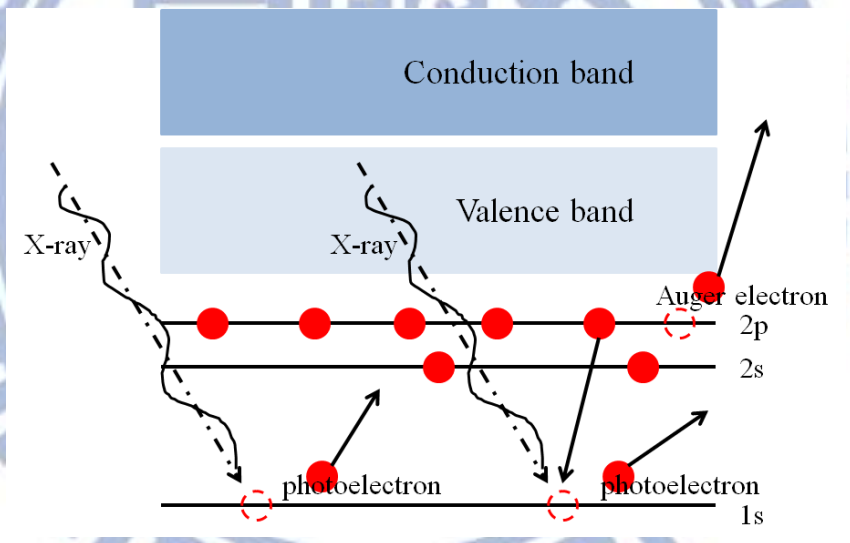

Figure 2.4 Scheme of photoelectrons and Auger electrons.

Besides, XPS is also a technique to investigate surface states of materials, based on the universal curve (Fig. 2.5), which describes the detection penetration depth in terms of electron mean paths. If the kinetic energy of photon electrons falls in the region 20-50 eV, electron mean free path is around 1 Å to 1 nm, that is, the

knocked-out electrons are primarily from 1 to 10 atom layers on the surface of a material. This is why XPS is very sensitive to the surface states.

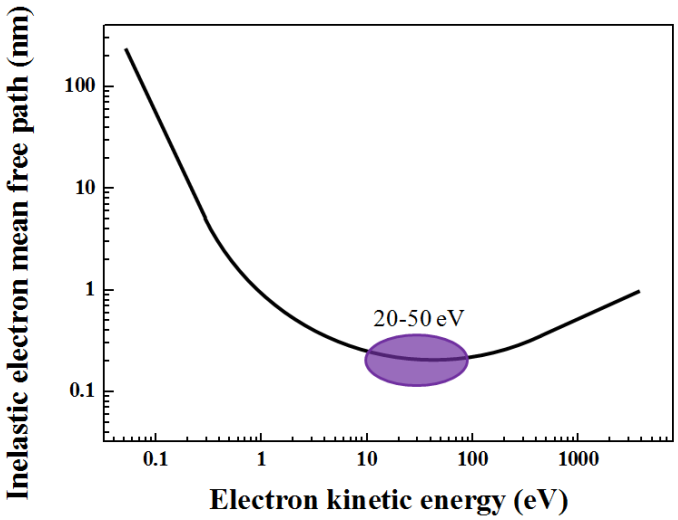

Figure 2.5 The universal curve: the electron mean free path is a function of electron kinetic energy[36].

2.3 X-ray Absorption Spectroscopy (XAS)

XAS is a powerful technique to detect the oxidation number, coordination number, neighbor atom types, bond distance and etc.[37-38]. XAS is an inelastic scattering: in this process, electrons at lower energy levels in atoms absorb photon energy to excited states when this photon energy encounters the absorption edge of these atoms. The absorption edge, simply speaking, is the absorption of the incident photon by a type of atoms when the energy difference between two energy levels of the atom is equal to the photon energy.

Here, only K-edge is discussed. K-edge means the absorption edge of electron transition from 1s to p orbital. The information of oxidation number appears in the energy shift of the K absorption edge. The reason is that the electrons in the K shell are more attracted by the nucleus due to the decreasing interference of outer electrons.

In one normalized XAS spectrum, before performing any fitting process, one can easily observe the change of oxidation states by K-edge shift. For K-edge absorption of a kind of atoms in a material, the higher the oxidation number the kind of atoms has, the higher energy the K-edge shifts to (Fig. 2.6). For instance, in Figure 2.6, it is observed that at the normalized intensity 0.5, the K-edge of $FeSO_4 \cdot 7H_2O$ has a relative higher energy (7121.1 eV), followed by those of Fe_3O_4 (7123.9 eV) and γ -Fe_2O_3 (7124.4 eV).

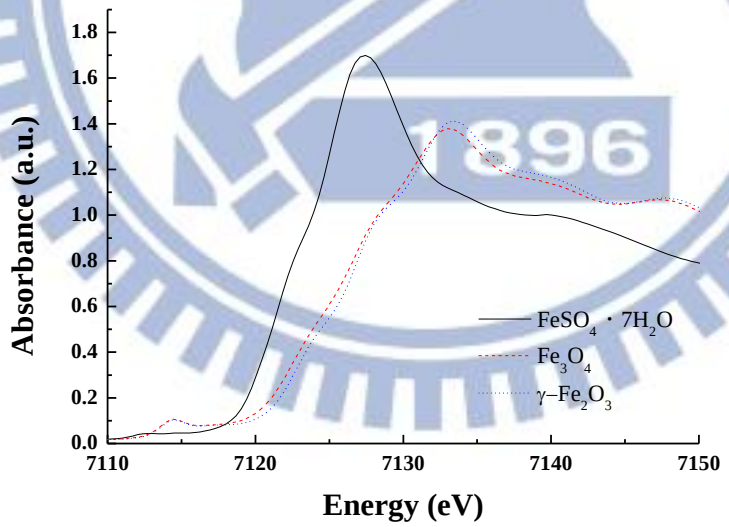

Figure 2.6 The normalized spectra of Fe K-edge for Fe_3O_4, γ -Fe_2O_3 and $FeSO_4 \cdot 7H_2O$ standard powders.

2.4 Synchrotron Radiation Infrared-Ray Microscopy (SRIRM)

Synchrotron radiation infrared-ray microscopy is base on Fourier Transformation Infrared-Ray spectroscopy (FTIR) and light microscopy. Light microscopy is used to visualize, localize and magnify structural details of interest in samples, while infrared-ray spectroscopy provides chemical information of the samples. For practical application of visualizing and detecting the microscopic world, the signal-to-noise (S/N) requirements should be taken into consideration. In order to obtain chemical mapping of samples, the aperture for IR entrance should be small enough, usually around 10 μm×10 μm or less, and this thereby leads to small S/N ratio. Synchrotron can overcome this problem, due to the small source size and sufficiently narrow ranges of angles of emission[39]. Besides, chemical mapping with high spatial resolution 10 μm can only be reached by SRIRM.

For the cell spectrum, a typical one is shown in Figure 2.7. This example is a normalized spectrum of A549 lung cancer cell. The absorption bands marked in Figure 2.7 are corresponding to chemical bonds in the A549 cell. In biological samples, most of the bands originate from DNA, proteins and lipids and the band positions maybe are a little different for different type of cells. Although the bands of DNA, proteins and lipids often overlap with each other, the marked bands in Figure 2.7 dominate in each constituent. Other bands are hard to identify where they arise from and should be needed for further investigation in each case. More information about SRIRM can be obtained in several reviews[40-41].

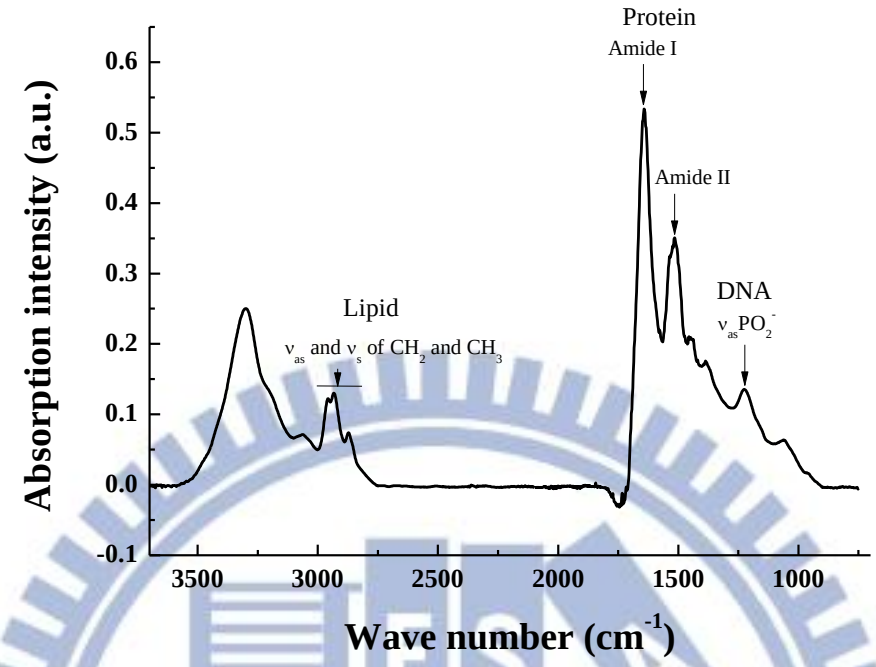

Figure 2.7 The normalized spectrum of A549 cells.

2.5 Cytotoxicity Measurement-MTT assay

Cytotocixity of MNPs is based on cell viability. Cell viability can be measured by counting individual live/dead cells step by step[42] or by assaying the whole cell population often by spectrophotometer (e.g., UV-visible). For the former, although it takes relatively more time, one can obtain the detailed cytotoxic information of individual cells, even in the early apoptosis stage[43]. Examples for this method are trypan blue[44] and staining live/dead cells by different fluorescence dyes including propidium iodide (PI), 7-aminoactinomycin (7-AAD), calcein AM and etc.[45]. On

the contrary, for the later, one can only exam the cell viability of the whole cell population without involvement of single cell analysis, but its advantage is relative rapid. Examples are lactate dehydrogenase (LDH) assay[46] and tetrazolium salts assay, both of which are based on metabolic activities of cells.

About tetrazolium salts assay, frequently used tetrazolium salts are 3-(4,5-dimethylthiazol-2-yl)-2,5-diphenyltetrazolium bromide (MTT), 3-(4,5-dimethylthiazol-2-yl)-5-(3-carboxymethoxyphenyl)-2-(4-sulphophenyl)-2H-tetrazolium (MTS), sodium 3'-[1-(phenylaminocarbonyl)-3,4-tetrazolium-bis-(4-methoxy-6-nitro) benzene sulphonic acid hydrate] (XTT), and Water soluble Tetrazolium salts (WSTs) derivatives. They are reduced into formazan, which is detected by spectrophotometer based on their maximum absorption wavelength.

Here, relatively more suitable although MTT assay is for many cell lines, care must be taken: Mitochondria has been recognized as the MTT reduction center because isolated mitochondria was proved to have the ability to reduce MTT since then MTT has been assumed to be reduced at mitochondria, but there are some evidences to prove that the cellular MTT reduction does not only occur at mitochondria, but also takes place in several regions in cells, and the end product formazan finally accumulates in endosomes/lysosomes[47]. Therefore, MTT assay result is determined by the rate of entocytosis and exocytosis. Consequently, for MTT assay measures endocytosis, a fundamental characteristic in the living cell, MTT assay as a measurement of cell viability is still valid[47].

MTT reduction mechanism has been studied with the CV technique and graphite

electrode as the working electrode by Marques et al.[48]. The following is the summary of MTT reduction, simply expressed as two steps: the first step (1) is a radical intermediate product MTT· is produced; in the second step (2), the intermediate product is reduced to formazan:

$$MTT + e^- \rightarrow MTT\cdot \quad (1)$$

$$MTT\cdot + e^- \rightarrow formazan^- \quad (2)$$

However, the second step (2) is affected by the pH value of the solution. MTT·, instead of processing the second step (2) directly, is rapidly protonated to form MTTH· (3), which is more easily reduced to formazan than MTT·. The final product formazam has been protonated twice (4) and (5), the process shown below:

$$MTT\cdot + H^+ \rightarrow MTTH^+\cdot \quad (3)$$

$$MTTH^+\cdot + e^- \rightarrow formazanH \quad (4)$$

$$formazanH + H^+ \rightarrow formazanH_2^+ \quad (5)$$

The standard potential for the reaction (1) at pH 7 is approximate -340 mV, while the formal potential for reaction (4) at pH 7 is -600 mV. These potential values change by -59 mV per pH. One can expect that MTT would spontaneously be reduced to formazan when it encounters any material with standard potential higher than -470 mV, roughly speaking. Therefore, one should notice that this would cause artificial formazan absorption signal in the MTT assay.

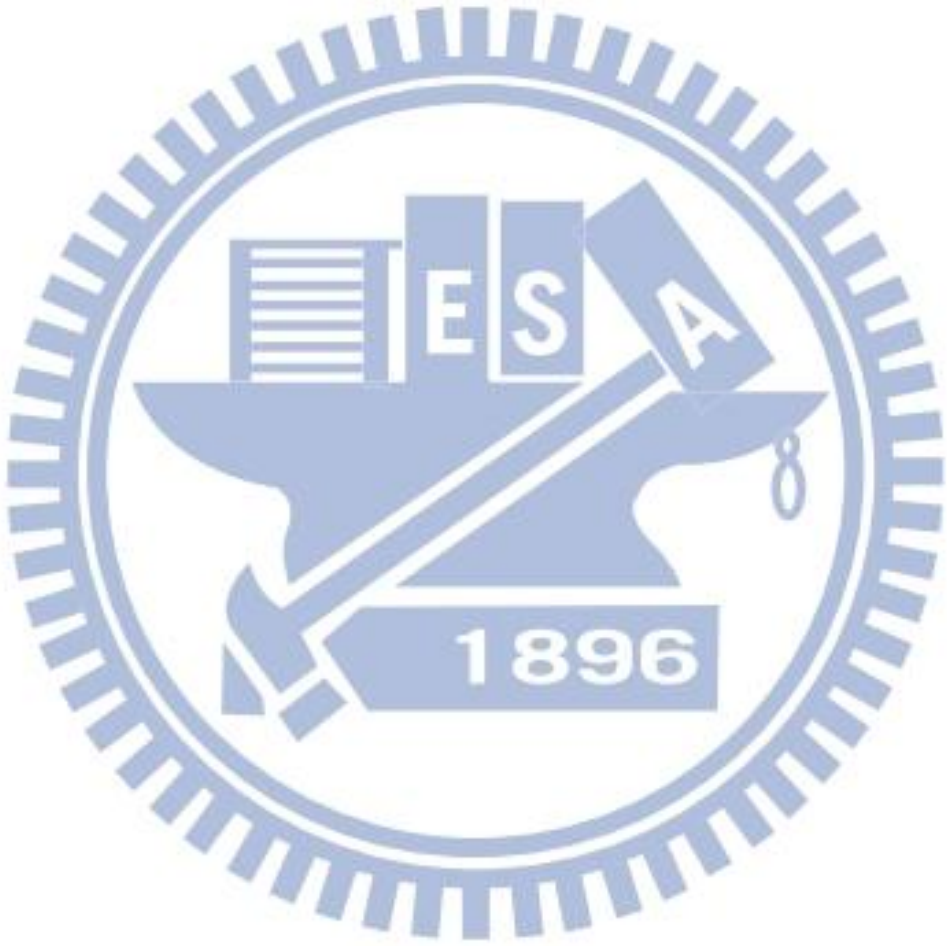

Chapter 3 Experimental

3.1 Fe_3O_4 and Fe_3O_4@SiO_2 MNPs

3.1.1 Synthesis of Fe_3O_4 and Fe_3O_4@SiO_2 MNPs

Fe_3O_4 MNPs were synthesized by coprecipitation method from ferrous sulfate ($FeSO_4 \cdot 7H_2O$) (2070-01, J. T. Baker) and ferric chloride hexahydrate ($FeCl_3 \cdot 6H_2O$) (12497, Alfa Aesar), this synthesis was modified from another paper[49]. 0.27 g $FeCl_3 \cdot 6H_2O$ was dissolved into 10 ml DI water in a glass beaker and into nitrogen-purged for 30 minutes, and then added with 0.139 g $FeSO_4 \cdot 7H_2O$. The solution was stirred at 80 ℃ in the hot bath for 10 minutes in the nitrogen atmosphere, followed by quickly adding 30 ml ammonia (NH_4OH) (9721-03, J. T. Baker) into the solution. The reaction was kept for 1 hour. After the synthesis, the solution was taken out of the hot bath, a magnet was used to attract Fe_3O_4 MNPs from the solution to the glass wall, and the supernatant was poured away and washed with DI water several times. Then, MNPs were washed by ethanol three times and concentrated to be kept in 55 ℃ in a baking oven overnight, and were grinded into powders for further usage (Fig. 3.1).

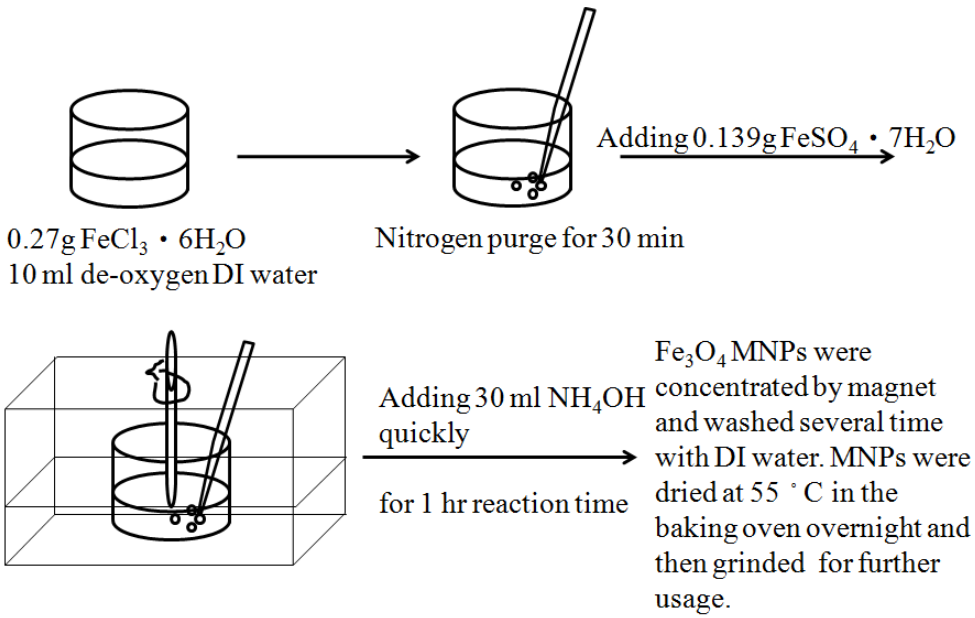

Figure 3.1 Fe_3O_4 MNPs synthesis process.

Stöber process was conducted to synthesize Fe_3O_4@SiO_2 MNPs [50]. 5.1 ml Triton X-100 (T8787, SIGMA) was mixed with 96 ml DI water, the solution was stirred for 5 minutes, and then was added with 1000 μl Tetraethyl orthosilicate (TEOS) (333859, SIGMA) and further stirred for 5 minutes. Meanwhile, a suspension containing 0.1 g Fe_3O_4 MNPs in 5 ml DI water was ultrasonic for 1 hour before being added into the solution. When the mixture of the Fe_3O_4 suspension and the solution was prepared, the solution was stirred for 5 minutes, then added with 30 ml 1-Hexanol (A18232, Alfa Aesar) and further stirred for 15 minutes. Until the solution was well mixed, 700 μl NH_4OH was added and the suspension was continuously stirred and remained at 35℃ for 7.5 hr. After the reaction, the suspension was centrifuged at 2000 rpm at 25℃ for 5 minutes to separate the two phases (oil and water) and to precipitate Fe_3O_4@SiO_2 MNPs to the bottom. A magnet was used to attract these MNPs and the supernatant was thrown away. The precipitates were washed with DI

water and ethanol (32221, SIGMA) several times and finally kept at 55 ℃ in the baking oven overnight. For further usage, Fe_3O_4@SiO_2 MNPs were grinded (Fig. 3.2).

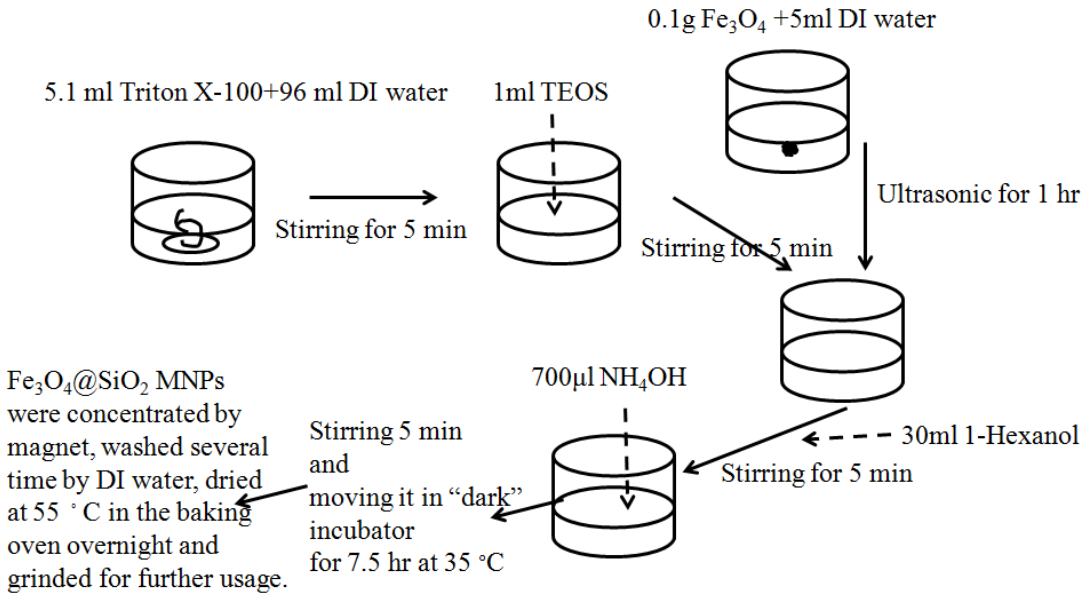

Figure 3.2 Fe_3O_4@SiO_2 MNPs synthesis process.

3.1.2 XRD-Phase

Phases of as-prepared Fe_3O_4 and Fe_3O_4@SiO_2 MNPs and the crystal sizes corresponding to the phases were measured with 16 KeV photon energy (wavelength: 0.7749Å) by X-ray diffraction (XRD), the synchrotron radiation beam light BL01C2 in National Synchrotron Radiation Research Center (NSRRC). The process of samples preparation was very simple: the powder was localized on a small 3M tape

and another small 3M tape was used to seal the powder in these two tapes, but one should assure that the amount of the powder be sufficient. The samples were pasted to a holder, which was adjusted to the proper position by manual. The operation parameters were controlled by Mar345 Control Software. The diffraction patterns of MNPs were recorded on 2D imaging plate and treated by Fit2D.

About the BL01C2, the beam spot size is 1mm (horizon)×1mm (vertical), the incident wavelength can be adjustable from 0.37 to 1.03Å by double Si crystal monochromators and diffraction pattern can be recorded by Mar345 imaging plate area detector or NaI(TI) point detector. More information about this beam light can be obtained in this website[51].

3.1.3 TEM-Size and Shape

The sample preparation process was simple. Fe_3O_4 and Fe_3O_4@SiO_2 MNPs suspensions with the concentration 1mg/ 1ml DI water were ultrasonic for 1 hr. Then, two copper grids coated with carbon film were put into the Fe_3O_4 MNPs and Fe_3O_4@SiO_2 MNPs suspensions, respectively, to let MNPs deposited onto the carbon film for around 3s. Particle size and the shape of Fe_3O_4 and Fe_3O_4@SiO_2 MNPs were observed by JEOL-JEM-2100F, 200kV.

3.1.4 XPS-Surface Property

To evaluate the surface composition and the surface states of Fe_3O_4 MNPs,

samples Fe_3O_4 and Fe_3O_4@SiO_2 MNPs put onto a gold substrate were examined by XPS , this is the synchrotron radiation beam light BL24A1 at NSRRC, because of its advantages of tunable incident photon energy and high intensity. Two primary incident photon energies, 650eV and 900eV, were used for survey scans because different elements have their optimal corresponding cross sections. In order to distinguish Auger electrons from photoelectrons, incident photon energies 625 eV and 875 eV were carried out.

About the BL24A1, the sample stage can be controlled in XYZ movements to find samples on a substrate (e.g. Si or Au). The beam spot size is 0.7×0.3 mm^2, the incident photon energy range is from 10 to 1500 eV and knocked-out electrons are analyzed by Clam4 one-channeltron Hemispherical Analyzer. More information about this beam light can be obtained in this website[51].

3.1.5 XAS-Oxidation State

In order to measure the oxidation state of Fe ions in the Fe_3O_4 and Fe_3O_4@SiO_2 MNPs, XAS, the synchrotron radiation beam light BL01C1 at NSRRC, was performed and the photon energy range was from 6912 eV to 8006 eV around the iron K-edge 7112 eV. There are two operation modes, transmission and fluorescence, and the suitable operation mode is dependent on the concentration of the samples. The data of the XAS were further normalized to compare each other by using software Athena[52].

About the BL01C1, the beam spot size is 0.9mm (horizon)×0.2mm (vertical),and

the incident photon energy range is from 6 to 33 kev adjusted by water-cooled, fixed-exit double Si crystal monochromators. More information about this beam light can be obtained in this website[51].

3.1.6 SQUID-Magnetic Property

36.5 mg Fe_3O_4 MNPs and 27.4 mg Fe_3O_4@SiO2 MNPs were put into two transparent plastic encapsulates for SQUID (MPMS5, QuantumDesign) measurements. The magnetic field H (unit: Oe) was conducted from -10000 Oe to 10000 Oe, and the magnetization of MNPs was measured. The temperature upon operation remained at room temperature around 300K. The magnetization was normalized with the weight of MNPs for comparison.

3.2 Cytotocixity of MNPs

3.2.1 Cell Culture-A549

The lung adenocarcinoma cells, A549 (BCRC number: 60074) were purchased from Food Industry Research and Development Institute (FIRDI) in the Republic of China (R.O.C, Taiwan). Cells were maintained in cell medium composed of 89.1 vol% RPMI 1640 (L0500, Biowest), 9.9 vol% Fetal Bovine Serum (S1520, Biowest) and 1 vol% Penicillin-Streptomycin (L0022, Biowest), and grown at 37℃ in a 5% CO_2 humidified environment. Trypsin-EDTA (L0931, Biowest) was used for the

dissociation of A549 cells from the flask.

3.2.2 MTT Assay

A549 cancer cells were seeded in some of 96 (8×12) wells (Fig. 3.3), and 100 μl cell solution (the cell concentration: 10^5 cells/ ml) was put into each well, those wells shown as dark areas; meanwhile, the gray areas represented 100 μl medium per well as the signal background of spectrophotometer (Emax Precision Microplate Reader, Molecular Devices) measurement, because MTT may be reduced by constituents in cell culture medium or the light may be scattered by MNPs. After 12 hr seeding time at 37℃ in a 5% CO_2 humidified environment, every well, except the wells of G and H rows, was injected with 10 μl of different MNPs suspentions with different concentrations (namely, 0, 0.625, 1.25, 2.5, 5, 10 μg/ 10 μl for A, B, C, D, E and F rows, respectively) of Fe_3O_4 MNPs (1~6 columns) and Fe_3O_4@SiO_2 MNPs (7~12 columns).

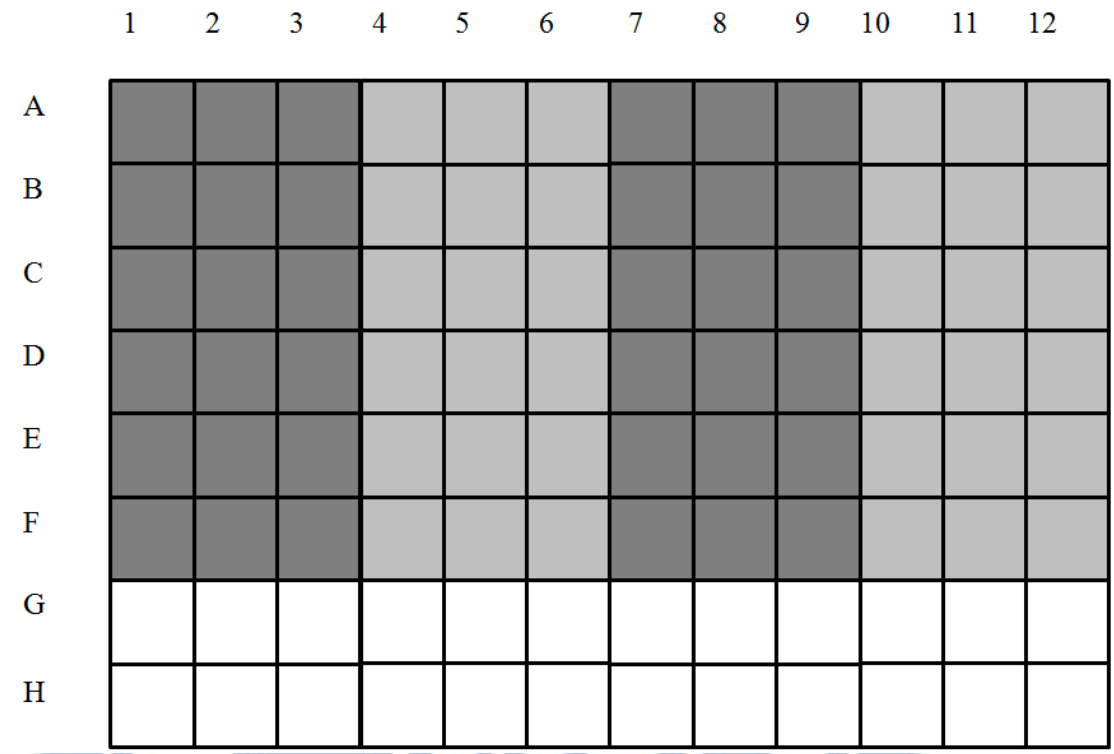

Figure 3.3 The 96 wells for MTT assay. Dark areas contained 10^4 cells per 100 μl, while gray region only contained medium as background for spectrophotometer measurement at 540 nm. A (as control): 0 μg MNPs per 110 μl (0 μg/ml), B: 10 μg MNPs per 110 μl (6 μg/ml), C: 5 μg MNPs per 110 μl (11 μg/ml), D: 2.5 μg MNPs per 110 μl (23 μg/ml), E: 1.25 μg MNPs per 110 μl (45 μg/ml) and F: 0.625 μg MNPs per 110 μl (91 μg/ml). Columns 1~6 are for Fe_3O_4 MNPs and columns 7~12 are for Fe_3O_4@SiO_2 MNPs.

More specifically, Fe_3O_4 MNPs suspension with 10 μg/ 10 μl was prepared by adding 5 mg into 5ml medium; before the addition of the medium, Fe_3O_4 MNPs were sterilized with dimethyl sulfoxide (DMSO) (D4540, SIGMA), of which the amount should not excess 1% of the volume of the final solution. In this case, the maximum amount of DMSO was 50 μl, approximate 1% in the MNPs suspension, but was less

than 1 % after 10 μl of the MNPs suspension was added into the well containing 100 μl cell solution or medium. This 50 μl DMSO was used to suspend 5mg Fe_3O_4 MNPs. Then, the suspension was ultrasonicated for 15 minutes, prior to addition of 5 ml cell culture medium. Different Fe_3O_4 MNPs concentrations were prepared by diluting Fe_3O_4 MNPs suspension (10 μg/ 10 μl) with the corresponding amount of medium. As a control group, 50 μl DMSO was added with 5 ml medium, expressed as 0 μg/ml. The process of the preparation of Fe_3O_4@SiO_2 MNPs suspensions was the same.

After A549 cells were treated with different MNPs concentration s for different treatment times, 2, 12, 24, 36 and 48 hr, 10 μl MTT (M2128, SIGMA) with concentration 500mg/200ml DI water was added into each well (except the wells of G and H rows) for 2 hr reaction time at 37℃ in a 5% CO_2 humidified environment in the incubator. The 96-wells plate was taken out to measure the absorption intensity of formazan reduced from MTT by mitochondria reductase.

Before measurement, small magnets, thus, were put under each well to attract MNPs in the solution to the bottom of wells, and then supernatant mediums in wells were drawn out by pipette. The reason to keep MNPs in wells is because MNPs can scatter the wavelength (540 nm) and consequently the absorption intensity may be affected, therefore keeping them in wells as background signals. Then each well was added with 100 μl DMSO , and it was shaken for 5 minutes and set into spectrophotometer to measure the absorption intensity of formazan. The cell viability was determined by the ratio of the absorption intensity of different conditions to the absorption intensity of control groups.

One A549 cell can become two A549 cells after its cell cycle τ. After a period of time t, the number of cells N can be calculated by this equation $N = N_0 \times 2^{t/\tau}$, where N_0 means the initial cell number. Since living cells can reduce MTT to formazan, the more living cells there are, the more produced formazam there are. Therefore, the absorption intensity P is proportional to the number of A549 cells N. That is said, N and N_0 can be replaced by P and P_0, and this equation finally becomes $P = P_0 \times 2^{t/\tau}$. Take natural log of this equation, it turns to $\ln P = \ln P_0 + (\frac{\ln 2}{\tau})\, t$, in which P_0 is initial formazan absorption intensity dependent on the experimental condition and τ is the cell cycle, and both of them could be determined from the intercept and the slope, respectively, from the figure "Natural log of absorption intensity versus time". Hence, the cell cycle life of the control group A549 cells and the MNPs-treated A549 cells for different MNPs treatment time can be calculated.

3.3 SRIR measurement

3.3.1 Sample Preparation

The IR samples were prepared by seeding A549 with 10^4 cells/ ml on Low-e slides for 12 hours. It is necessary to ensure that Low-e slides should be disinfected for at least 30 minutes under ultra UV. After the seeding process, each IR sample was vertically put into cell culture medium, and some of them subsequently was added with the Fe_3O_4 MNPs or Fe_3O_4@SiO_2 suspension with concentration 10 μg/ 10 μl for treatment time 12, 24 and 36 hr. Others were added with different MNPs (Fe_3O_4 or

Fe_3O_4@SiO_2) suspension concentrations of 1.25 and 10 μg/ 10 μl for the same treatment time 36 hr. These IR samples were taken out, after the MNPs treatment time, to be washed with 0.01M PBS (X0515, Biowest) three times, and were treated with 2.5% glutaraldehyde (G7651, SIGMA) for 1 hr to preserve the morphology and contents of cells intact, followed by dehydration process: DI water for three times, 50% ethanol three times each time for 10 min, as well as 70% and 90% ethanol, 100% ethanol three times each time for 15 min, 100% acetone (9006-03, J. T. Baker) twice each time for 5 min, and finally dried and kept in a dry box.

3.3.2 Data Procedure and Analysis

In order to observe the change of the relative amount of biological components (e.g., protein, lipid, etc.) of cells, SRIR beam light, the synchrotron radiation beam light BL14A1 at NSRRC, was performed to measure the absorption intensity of a single cell from wave number 650 cm^{-1} to 4000 cm^{-1} by localizing it in a 50×50 μm^2 aperture for 1024 scans and spectral resolution of 4 cm^{-1}. Spectra were collected in reflection mode. Prior to the cell spectra collection of each sample, a background sample was taken at a free-cell place on the L-e slide IR sample and subtracted from the spectrum of cell on the same IR sample. Spectra were analyzed by Omnic 7.3.

The total number of cells for IR measurement per sample was 50. The spectrum of each cell, after the background subtraction, was normalized by its area under the absorption curve. Therefore, the mean absorption of the total 50 cells was calculated for IR analysis. Chemical mapping images of individual cells were recorded with 15× 15 μm^2 aperture, spectral resolution 4 cm^{-1} and step size 10 μm.

About the BL14A1, the incident beam spot size is 10 μm (horizon)×13 μm (vertical), the photon energy range is from 4000 to 600 cm-1 and IR spectra are collected by liquid nitrogen cooled HgCdTe Infrared detectors. More information about this beam light can be obtained in this website[51].

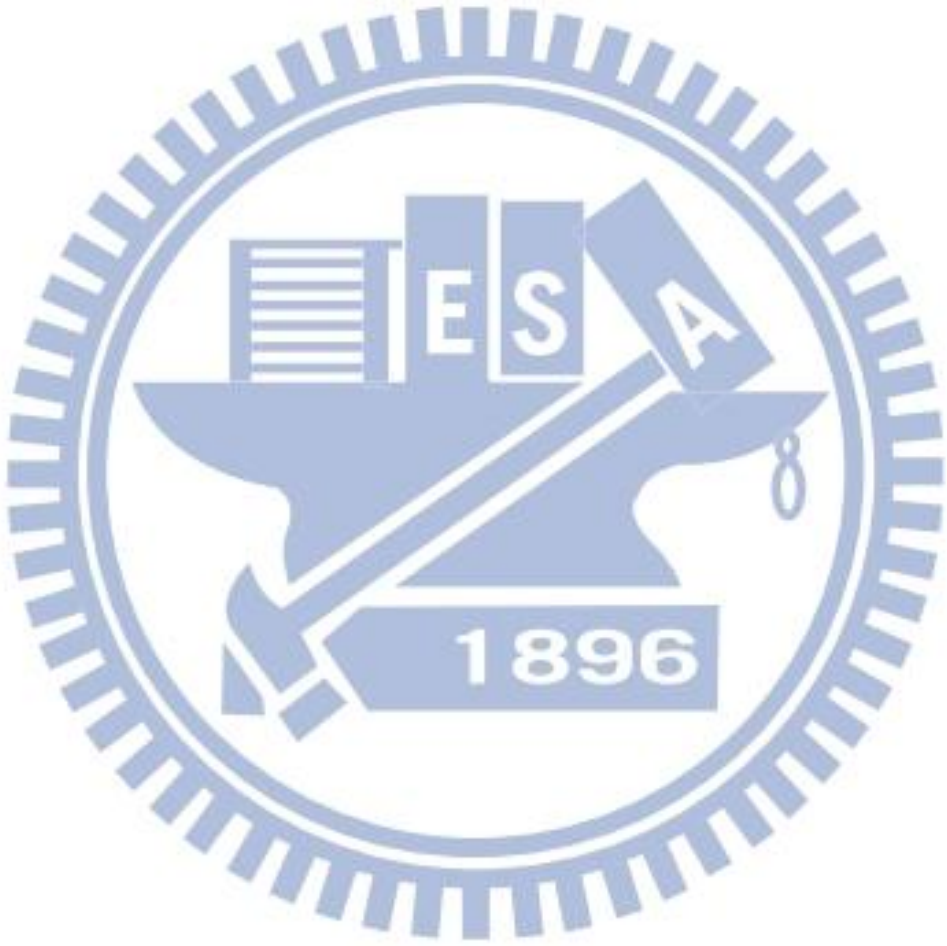

Chapter 4 Results and Discussion

4.1 MNPs Characterization

4.1.1 XRD-Phase Determination and Crystal Size

Figure 4.1 shows the XRD pattern of as-prepared Fe_3O_4 and Fe_3O_4@SiO_2 MNPs. From the Figure 4.1, the 2θ scan for the sample of Fe_3O_4 and Fe_3O_4@SiO_2 MNPs is quite similar to each other. The crystalline structures of (111), (200), (311) and (400) are clearly observed at the peak position of 9.2°, 15.1°, 17.1° and 21.4°, respectively. It indicates the as-prepared Fe_3O_4 and Fe_3O_4@SiO_2 MNPs samples contains phase Fe_3O_4. Moreover, the crystalline structures of (104) and (018) are observed, which means the samples have a few composition of the α-Fe_2O_3 phase[53]. From the peak of full width at half maximum (FWHM), two sets of FWHM with, in radian, 0.009 at (200) for Fe_3O_4 phase and 0.00227 at (104) for α-Fe_2O_3 phase are observed. Based on the Scherrer equation $D = \frac{K\lambda}{\beta \cos\theta}$ and K is 0.9 (assume the shape is spherical) , for (200) of Fe_3O_4 phase and θ is 7.513, the crystal size of Fe3O4 phase is 7.9 nm, while for (104) of α-Fe_2O_3 phase and θ is 8.273, the crystal size is 31.6 nm. From Figure 4.1, the crystalline structures of Fe_3O_4 phase and α-Fe_2O_3 phase are clearly observed. However, SiO_2 diffraction peaks in the Fe_3O_4@SiO_2 MNPs are not observed, suggesting the SiO_2 layer on Fe_3O_4 MNPs is amorphous.

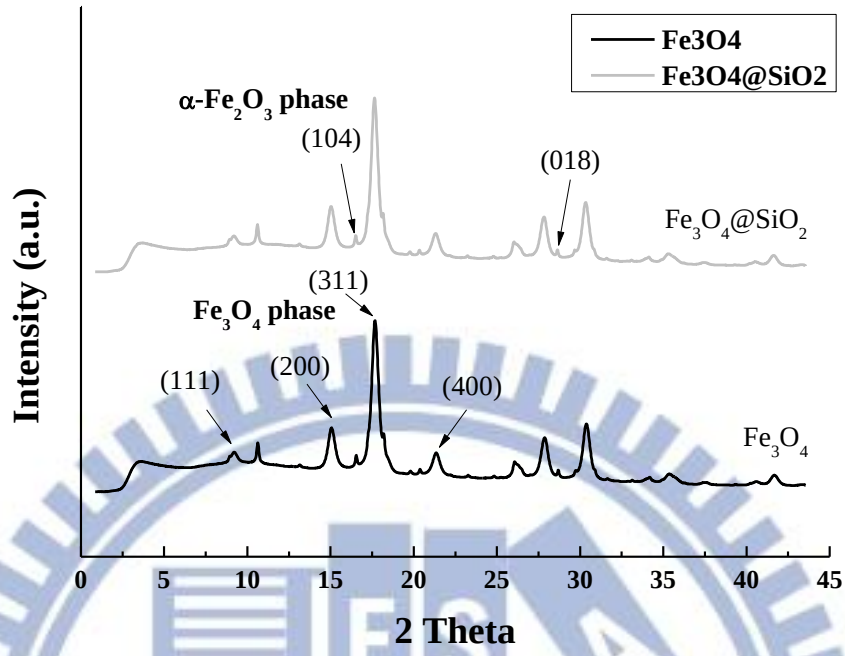

Figure 4.1 The powder XRD patterns of Fe_3O_4 MNPs and Fe_3O_4@SiO_2 MNPs.

4.1.2 TEM-Particle Size and Shape

Figure 4.2 displays the TEM image of Fe_3O_4 MNPs. The shape of Fe_3O_4 MNPs is not simply spherical, but irregular (Fig. 4.2(a) and (b)), and this result provides an evidence for XRD analysis in which the shape factor in Scherrer equation is assumed to be 0.9. These MNPs appear aggregated, and this phenomenon may be caused by surface tension when water evaporated during the sample preparation or by the nature of the Van der Waal force. From the dynamic scattering light analysis, the mean hydrodynamic diameter of Fe_3O_4 MNPs in DI water is around 105.7 nm, and this suggests that Fe_3O_4 MNPs are aggregated in DI water, not individual nanoparticles

suspending in the solution. From Figure 4.2(c), the lattice pattern of Fe_3O_4 MNPs is clearly observed, and this means that Fe_3O_4 MNPs are exactly crystalline. Two plane distances are marked, and they are around 2.5 and 4.545 Å, as the same as previous studies[54-55]. The former plane distance is corresponding to the diffraction peak (311) in the XRD pattern and the later is related to the diffraction peak (111) (Fig. 4.1). Figure 4.2(d) shows that almost Fe_3O_4 MNPs have particle size in the range 6~11 nm, consistent with the crystal size of Fe_3O_4 obtaining from the XRD pattern. Besides, MNPs with particle size larger than 20 nm are rarely observed in TEM images, and this indicates that the amount of α -Fe_2O_3 phase in the samples is very small.

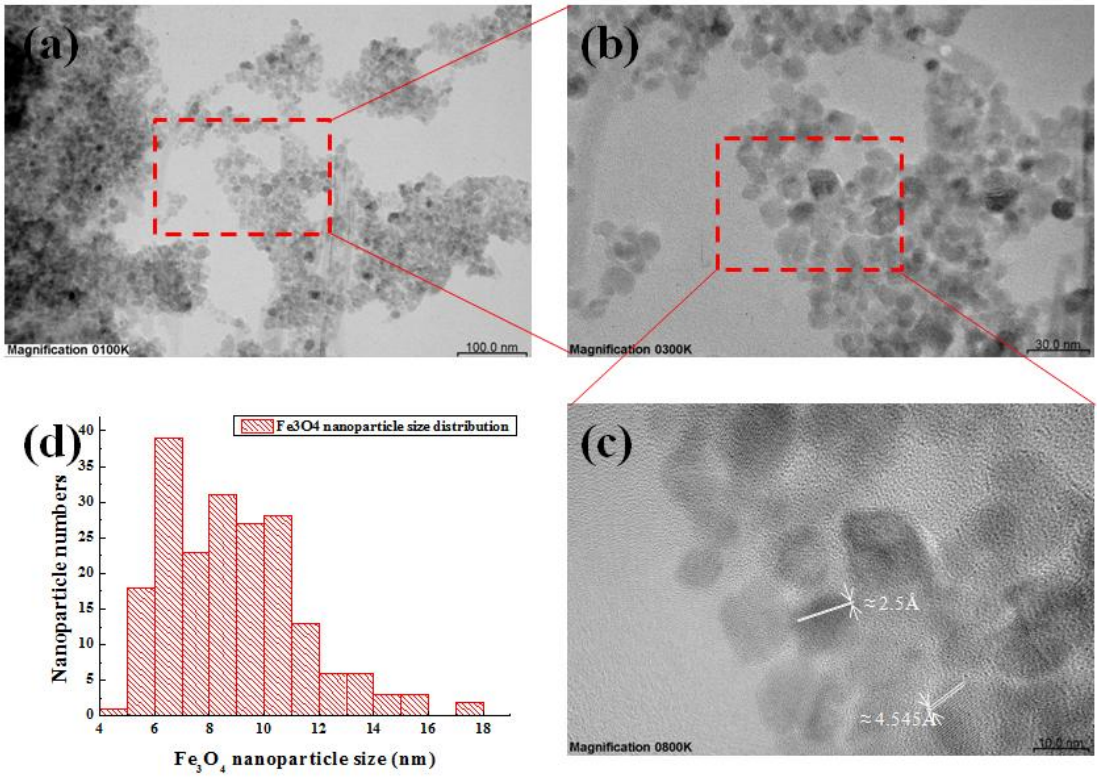

Figure 4.2 Fe_3O_4 MNPs TEM Images (a) 10^5 magnification. (b) 3×10^5 magnification of the rectangular region in (a). (c) 8×10^5 magnification of the rectangular area in (c). (d) MNPs particle size distribution based on (a).

Figure 4.3 displays the TEM image of Fe_3O_4@SiO_2 MNPs. Fe_3O_4@SiO_2 MNPs have not a typical core shell structure, which means one particle has one outer shell. Fig. 4.3(a) shows that several Fe_3O_4 MNPs are aggregated and covered by SiO_2 layer, or individual Fe_3O_4 MNPs coated with SiO_2 were aggregated to form a large cluster. From the dynamic scattering light analysis, the mean hydrodynamic diameter of Fe_3O_4@SiO_2 MNPs in DI water is approximate 220 nm. The lattice of Fe_3O_4 still can be observed when coated with SiO_2. From Figure 4.3(b), it is shown that the SiO_2 layer is amorphously deposited on the outer of Fe_3O_4 MNPs clusters, and this result is accordant with the analysis result of the XRD pattern.

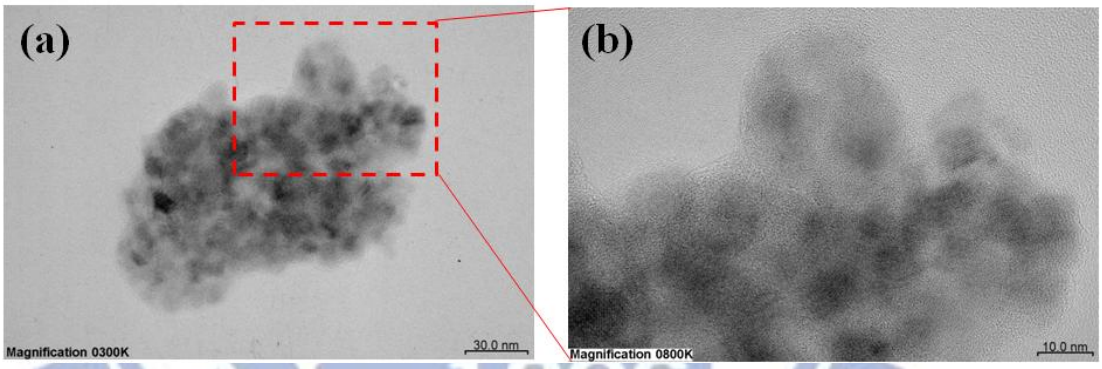

Figure 4.3 Fe_3O_4@SiO_2 MNPs TEM images (a) 3×10^5 magnification. (b) 8×10^5 magnification of the rectangular area in (a).

4.1.3 XPS-Surface State of MNPs

Since there exists different phases, Fe_3O_4 and α-Fe_2O_3, in the Fe_3O_4 MNPs and Fe_3O_4@SiO_2 MNPs samples, there is a possibility that γ-Fe_2O_3 ($[Fe^{3+}]_{Td}[Fe^{3+}_{5/3}V_{1/3}]_{Oh}O_4$ where Td means tetrahedral sites while Oh means octahedral sites; V means vacancies) phase maybe also exists in the Fe_3O_4 and

Fe_3O_4@SiO_2 MNPs samples. The challenge is that this phase could not be distinguished from the Fe_3O_4 ($[Fe^{3+}]_{Td}$ $[Fe^{2+}Fe^{3+}]_{Oh}O_4$) phase simply by the XRD pattern because of the similar XRD patterns[56-57]. This is because the difference between γ-Fe_2O_3 ($[Fe^{3+}]_{Td}[Fe^{3+}_{5/3}V_{1/3}]_{Oh}O_4$) and Fe_3O_4 ($[Fe^{3+}]_{Td}$ $[Fe^{2+}Fe^{3+}]_{Oh}O_4$) is the lack of Fe^{2+} in the octahedral sites in γ-Fe_2O_3 phase. This subtle difference is hard to be detected by XRD technique. Therefore, XPS analysis is conducted to determine the phases more accurately[58], since it is more sensitive to oxidation states of ions in a material .

Figure 4.4 displays the XPS of Fe_3O_4 and Fe_3O_4@SiO_2 MNPs. From Figure 4.4, two primary peaks Fe2p with binding energy 711.4 eV ($Fe2p_{3/2}$) and 725.2 eV ($Fe2p_{1/2}$), respectively, for both MNPs are observed ,and for Fe_3O_4@SiO_2 MNP, between two primary peaks is an evident peak, 719.7 eV, called satellite, which is separated from the first primary $Fe2p_{3/2}$ peak around 8 eV[59-60]. For pure Fe_3O_4, there should not exist a satellite between the two primary peaks $Fe2p_{1/2}$ and $Fe2p_{3/2}$[59-60]. Nevertheless, in our Fe_3O_4 MNPs sample, a small satellite peak is observed and this maybe indicates that the surface of Fe_3O_4 MNPs is oxidized to higher oxidation number. This is possible because of more stability of γ-Fe_2O_3 phase without the iron ion being reduced form Fe^{2+}. Compared to Fe_3O_4 MNPs, there is an obvious satellite for Fe_3O_4@SiO_2 MNPs, which likely suggests that Fe ion is further oxidized to much higher oxidation number after reacting with SiO_2. As XPS is very sensitive to the surface state, another technique, XAS, thus, is performed to examine its bulk oxidation number.

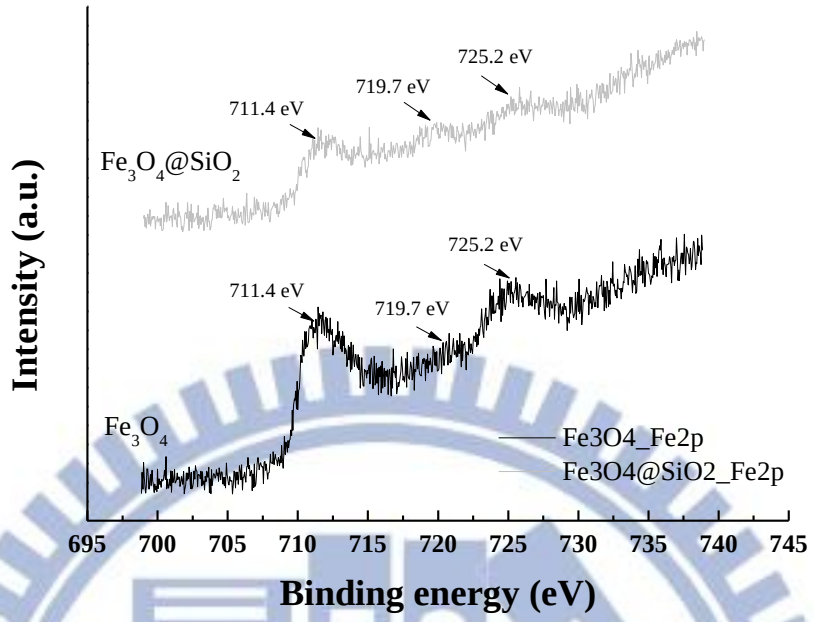

Figure 4.4 XPS Fe2p spectra of Fe_3O_4 MNPs and Fe_3O_4@SiO_2 MNPs.

4.1.4 XAS Analysis-Oxidation State

Fe K-edge of $FeSO_4 \cdot 7H_2O$ (one of Fe_3O_4 MNPs precursors), α-Fe_2O_3, γ-Fe_2O_3, Fe_3O_4 standard powders and the sample Fe_3O_4 MNPs were examined by XAS and shown in Fig. 4.5. The oxidation number is related to the position of K-edge (1s $\rightarrow$p), and the higher the oxidation number is, the higher energy the edge shifts toward. As seen in Figure 4.5, for the precursor, due that $FeSO_4 \cdot 7H_2O$ contains Fe^{2+}, its K-edge position is thus lower than the others, while γ-Fe_2O_3 includes Fe^{3+} and its K-edge is thereby higher than the others. It is obvious that the K-edge of Fe_3O_4 MNPs is closer to that of Fe_3O_4 standard powder and this indicates that the oxidation number of as-prepared Fe_3O_4 MNPs is much similar to Fe_3O_4, not to α-Fe_2O_3 nor to γ-Fe_2O_3. Therefore, Fe_3O_4 MNPs primarily contain Fe_3O_4 phase, not γ-Fe_2O_3. Furthermore, in order to check whether the phase of Fe_3O_4 MNPs is Fe_3O_4 or not, first

derivative of Fig. 4.5 is adopted as shown in Figure 4.6. It is observed that the first derivative curves of α-Fe_2O_3 phase and the precursor $FeSO_4 \cdot 7H_2O$ are very different from others. Although the first derivative curve of γ-Fe_2O_3 is similar to that of Fe_3O_4 MNPs, the region between 7122 eV and 7126 eV in Fe_3O_4 MNPs is relatively more similar to that in Fe_3O_4 standard powder. Thus, as-prepared Fe_3O_4 MNPs are exactly Fe_3O_4 phase. Also, from the pre-edge (Fig. 4.5), Fe_3O_4 and γ-Fe_2O_3 standard powders show a peak around 7114 eV, whereas α-Fe_2O_3 had a small broader peak around 7115 eV. For Fe_3O_4 MNPs, there does not exhibit a broad peak at 7115 eV, but exists a peak as the same as Fe_3O_4 and γ-Fe_2O_3 powder standards do. Therefore, from the experimental result, it indicates that Fe_3O_4 MNPs contain a very small amount of α-Fe_2O_3 phase, the same result as TEM images (Fig. 4.2).

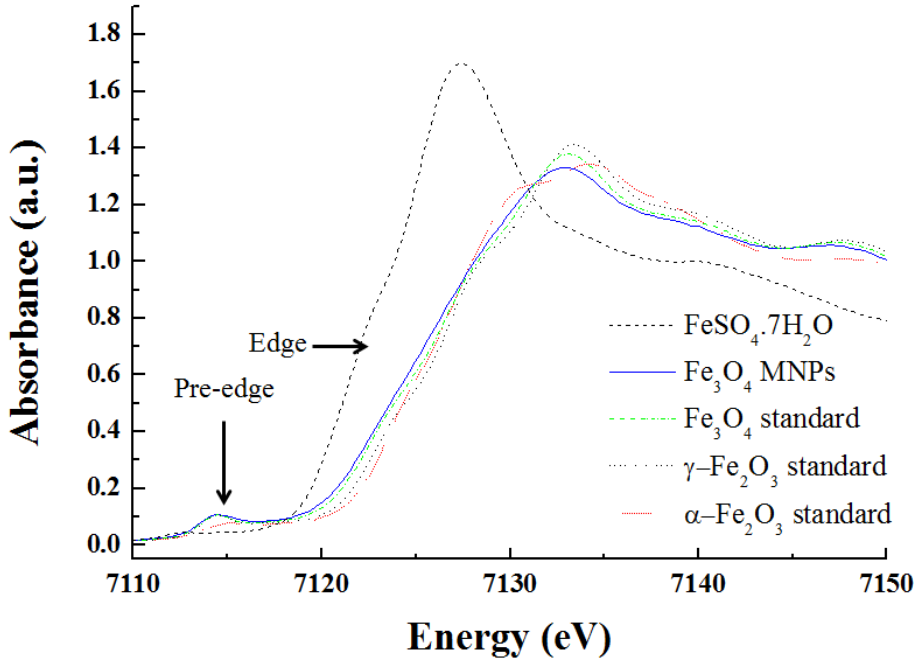

Figure 4.5 Fe K-edge: materials including the precursor $FeSO_4 \cdot 7H_2O$, standard powders, α-Fe_2O_3, γ-Fe_2O_3, Fe_3O_4 and sample Fe_3O_4 MNPs.

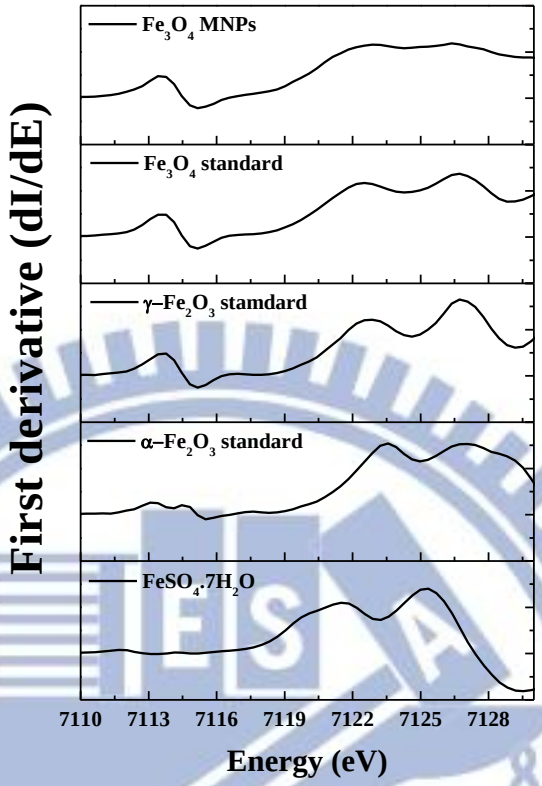

Figure 4.6 First derivative of XAS spectrum (Fig. 4.5) with respect to energy.

4.1.5 SQUID-Magnetic properties

Figure 4.7 shows the SQUID measurement of both Fe_3O_4 and Fe_3O_4@SiO_2 MNPs under room temperature 300K. Although there is a small magnetic hysteresis loop is observed in Fe_3O_4 MNPs, it is relative small. Hence, we think they are primarily superparamagnetic. As the size of these MNPs reduces to a dimension smaller than its theoretical critical single domain size 25 nm[61]or 128 nm[1] for Fe_3O_4, every MNP forms a big single magnetic momentum. These magnetic momentums could attract each other if there were no external forces preventing them.

However, the thermal energy at room temperature is sufficient to overcome this magnetic attraction among these magnetic momentums, thereby contributing to their superparamagnetic property. For Fe_3O_4 MNPs with approximate 10 nm in this case, that's why MNPs are superparamagnetic. The saturation magnetization for Fe_3O_4 MNPs and $Fe_3O_4@SiO_2$ MNPs are 51.5emu/g and 45emu/g, respectively, similar to the previous work by coprecipitation in sonochemical synthesis method[62]. The smaller saturation magnetization for $Fe_3O_4@SiO_2$ MNPs is due to the contribution of the nonmagnetic component SiO_2.

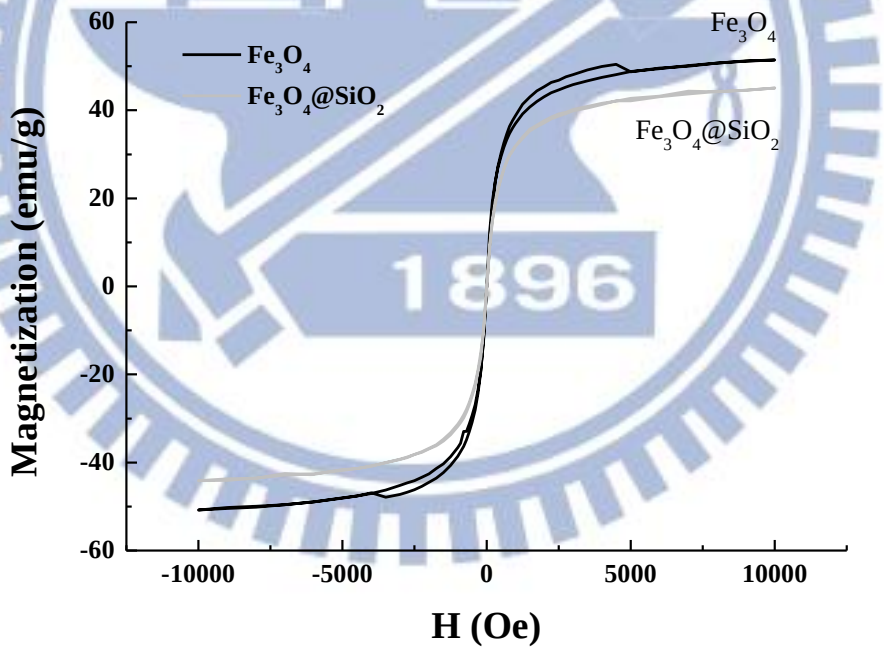

Figure 4.7 Fe_3O_4 MNPs and $Fe_3O_4@SiO_2$ MNPs SQUID measurement

4.2 Cytotoxicity of MNPs in cells

4.2.1 Mitochondria Reductase Activity

Table 4.1 displays the absorption intensity in raw data of formazan formation by MTT reduction of 48 hr-MNPs-treated A549 cells, corresponding to Fig. 3.3. In the columns 1~3 and 7~9, the absorption intensities are higher than the others, because there were cells in these wells, these cells had been treated with different MNPs concentrations from rows A to F: 0, 6, 22, 23, 45 and 91 μg/ml (corresponding to the MNPs suspension concentrations 0, 0.625, 1.25, 2.5 and 10 μg/10 μl). In the columns 4~6 and 10~12, these data as background signals, shown as bold in table 4.1, for different conditions are absorption intensities for these wells containing different amounts of MNPs, 0, 0.625, 1.25, 2.5, 5 and 10 μg from A to F rows. One can observe that these background signals climb as MNPs concentration increases. This maybe results from MTT reduction via reductive molecules[47] in medium through MNPs catalysis[63], maybe originates from MTT reduction by NPs with redox potential higher than that of MTT[64], or maybe arises from scattering by MNPs. The SiO_2 layer of Fe_3O_4@SiO_2 MNPs cannot, however, be oxidized further. Therefore, the increase of the absorption intensity from low MNPs concentration to high MNPs concentration maybe originates from the lost of signal due to light scattered by MNPs or MTT reduction by MNPs catalysis. No matter how these background signals occur, they serve as background signals for subtraction.

Table 4.1 The absorption intensity raw data (48hr MNPs treatment time) of formazan dissolved in DMSO detected under wavelength 540 nm. Columns 1~6 are for Fe_3O_4 MNPs cytotoxicity analysis and columns 7~12 are for Fe_3O_4@SiO_2 MNPs cytotoxicity analysis. Bold denotes the background signal for subtraction.

	1	**2**	**3**	**4**	**5**	**6**	**7**	**8**	**9**	**10**	**11**	**12**
A	1.161	0.978	0.824	**0.048**	**0.047**	**0.046**	0.95	1.372	1.261	**0.043**	**0.045**	**0.046**
B	1.216	1.123	0.947	**0.047**	**0.047**	**0.049**	1.195	0.778	1.094	**0.052**	**0.049**	**0.046**
C	0.757	0.852	0.99	**0.048**	**0.048**	**0.048**	1.043	1.005	0.864	**0.049**	**0.048**	**0.05**
D	1.022	0.922	1.004	**0.057**	**0.051**	**0.051**	1.155	0.9	0.813	**0.058**	**0.062**	**0.057**
E	0.744	0.749	0.668	**0.062**	**0.067**	**0.067**	0.864	0.971	0.822	**0.074**	**0.085**	**0.071**
F	1.094	0.737	0.921	**0.093**	**0.09**	**0.09**	1.097	0.809	1.139	**0.104**	**0.135**	**0.132**
G	0.041	0.042	0.041	0.04	0.042	0.042	0.038	0.039	0.042	0.04	0.038	0.04
H	0.039	0.038	0.046	0.042	0.042	0.042	0.038	0.038	0.04	0.039	0.038	0.04

Figure 4.8 displays that the absorption of formazan formed from MTT reduction by A549 cells at various applied MNPs concentrations under different MNPs treatment times. When A549 cells are treated with MNPs for 2 hr and 12 hr, it shows that absorption intensity remains almost the same with different MNPs concentrations. This indicates that mitochondria reductase activity does not decay during these

periods of time. However, it is observed that absorption intensity starts to decline slightly with MNPs concentrations after 24 hr MNPs treatment time and becomes more dramatic with MNPs concentrations when the MNPs treatment time is longer. Although the absorption begins to decrease with MNPs concentrations after 24 hr, the absorption intensity for a constant concentration rises with time. Because the formazan absorption intensity is proportional to living cell number, the increase of absorption intensity means the number of cells rises. Therefore, this means that even under MNPs treatment, the number of A549 cells grows steadily.

Interesting is that from the data of Figure 4.8 and the equation $\ln P = \ln P_0 + (\frac{\ln 2}{\tau})\, t$, it is calculated that the cell cycle life of control group A549 cells is around 19 hr, whereas the cell cycle life of A549 cells increases to almost 22~24 hr if the cells are treated with Fe_3O_4 MNPs or $Fe_3O_4@SiO_2$ MNPs, shown in Table 4.2. This result indicates that the rate of proliferation of A549 cells slows down when A549 cells are treated with MNPs. The reason why cells prolong their cell cycle life maybe results from the DNA structure change, in this situation, cells remain at G1 phase and it takes some time for enzymes to restore the structure-changed DNA before entering into S phase. The above discussion is just one possible explanation. Another possibility is that instead of prolonged cell cycle life, A549 cells treated with MNPs die out, thereby leading to the decline in the absorption intensity of formazan with MNPs concentrations at a given MNPs treatment time.

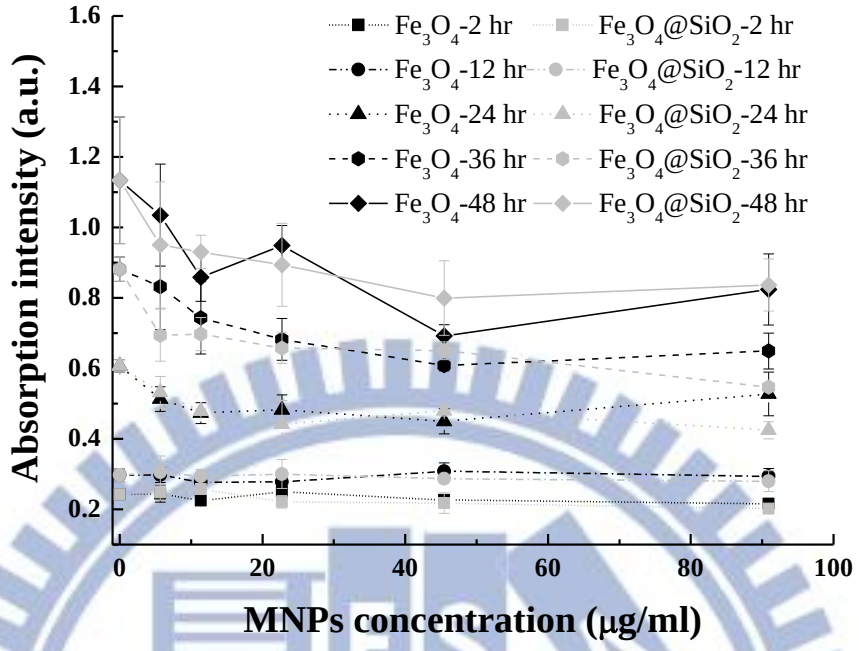

Figure 4.8 The absorption intensity of formazan formed from MTT reduction by A549 living cells versus the treatment of MNPs concentrations at different MNPs treatment times.

Table 4.2 The cell cycle life of the control group A549 cells and the MNPs-treated A549 cells. R means the reliability coefficient.

MNPs Concentration (μg/ml)	**The cell cycle of A549 cells treated with Fe_3O_4 MNPs (hr)**	**The cell cycle of A549 cells treated with Fe_3O_4@SiO_2 MNPs (hr)**
0	19 (R^2=0.96)	19 (R^2=0.96)
6	20 (R^2=0.97)	23 (R^2=0.98)
11	22 (R^2=0.96)	23 (R^2=0.98)
23	22 (R^2=0.97)	23 (R^2=0.99)
45	28 (R^2=0.96)	24 (R^2=0.97)
91	23 (R^2=0.95)	23 (R^2=0.99)

4.2.2 Cell Viability

Fe_3O_4 MNPs show almost no cytotoxicity to A549 cells for every MNPs concentration during 24 hr MNPs treatment time, as shown in Figure 4.9. This result is in agreement with other studies showing low toxic effect of Fe_3O_4 in this period of time[29, 65] because of low ROS production during these periods. But after 24 hr MNPs treatment time, cell viability of A549 cells is 84 % when A549 cells are treated with the lowest MNPs concentration (6 μg/ml)and even lower than 72 % when cells

are exposed to the highest MNPs concentration (91 μ g/ml). This indicates that cell viability of MNPs-treated A549 cells is time-dependent, almost close to 100 % during 12 hr, but decreasing after 24 hr. In addition, cell viability of MNPs-treated A549 cells are also concentration-dependent, declining with MNPs concentration for the same MNPs treatment time.

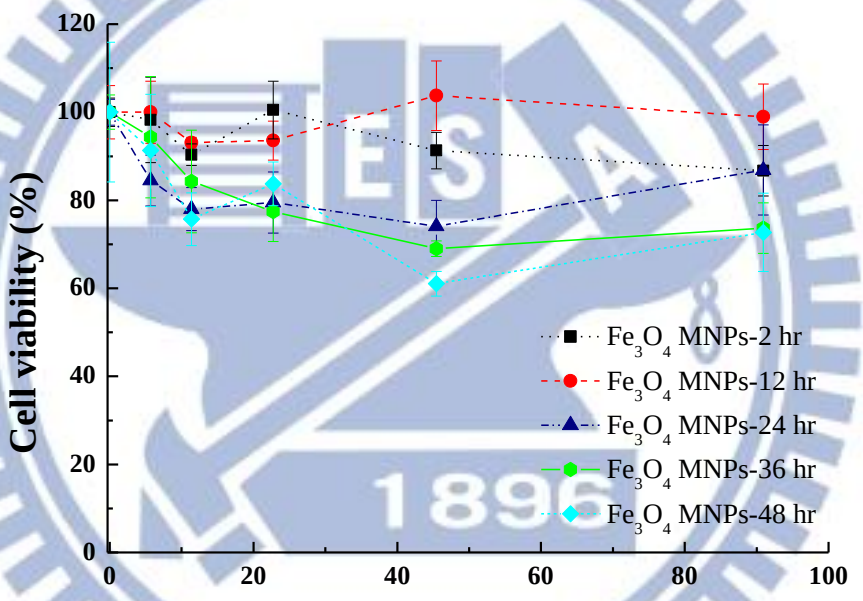

Figure 4.9 The cell viability based on MTT assay for A549 treated with different Fe_3O_4 MNPs concentrations for 2, 12, 24, 36 and 48 hr.

Figure 4.10 exhibits the cytotoxicity of Fe_3O_4@SiO_2 MNPs to A549 cells. During 24 hr MNPs treatment time, Fe_3O_4@SiO_2 MNPs shows no apparent

cytotoxicity to A549 cells, while after 24 hr MNPs treatment time, they show increased cytotoxicity with MNPs concentrations, similar to the result of Fe_3O_4 MNPs. Comparison of both cell viabilities caused by Fe_3O_4 MNPs and Fe_3O_4@SiO_2 MNPs shows that cytotoxicity may be independent of the composition of Fe_3O_4 MNPs and Fe_3O_4@SiO_2 MNPs in this case. However, in this moment, whether MNPs enters into A549 cells or not is unknown. These similar results suggest that cell viability of MNPs-treated A549 cells is a characteristic of A549 cells when A549 cells are exposed upon outside triggers.

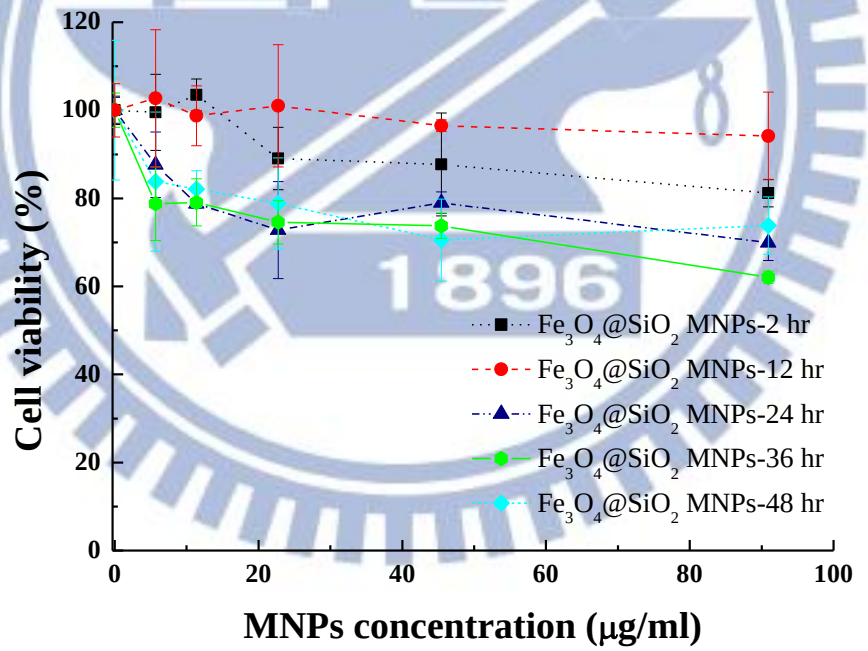

Figure 4.10 The cell viability based on MTT assay for A549 treated with different concentrations Fe_3O_4@SiO_2 MNPs for 2, 12, 24, 36 and 48 hr.

4.3 SRIR Spectra and Images of A549 treated by MNPs

4.3.1 A549 treated with Fe_3O_4

4.3.1.1 Treatment Time Effect

Figure 4.11 shows the normalized SRIR spectra of A549 cells after Fe_3O_4 MNPs treatment in different time periods at applied MNPs concentration of 91 μg/ml. The band around 1218 cm^{-1} originates from the asymmetric phosphodiester groups PO_2^- stretching vibration mode mostly from DNA. At 1641.1 cm^{-1}, the amide I band is observed, from the C=O stretching vibration modes of the protein amide bonds. The bands at 1513.8 cm^{-1} is from the amide II band, a combination of the N-H bending vibrations and C-N stretching vibrations of the amide bonds. The band around 2800~3000 cm^{-1} arises from the symmetric and asymmetric C-H stretching modes of CH_2 (2856 and 2933 cm^{-1}) and CH_3 (2871 and 2956 cm^{-1}) groups dominant in lipids. The region around 3600 cm^{-1} originates from both stretching modes of the O-H and N-H in water, proteins, and polysaccharides. The spectra for each condition are subtle different from each other.

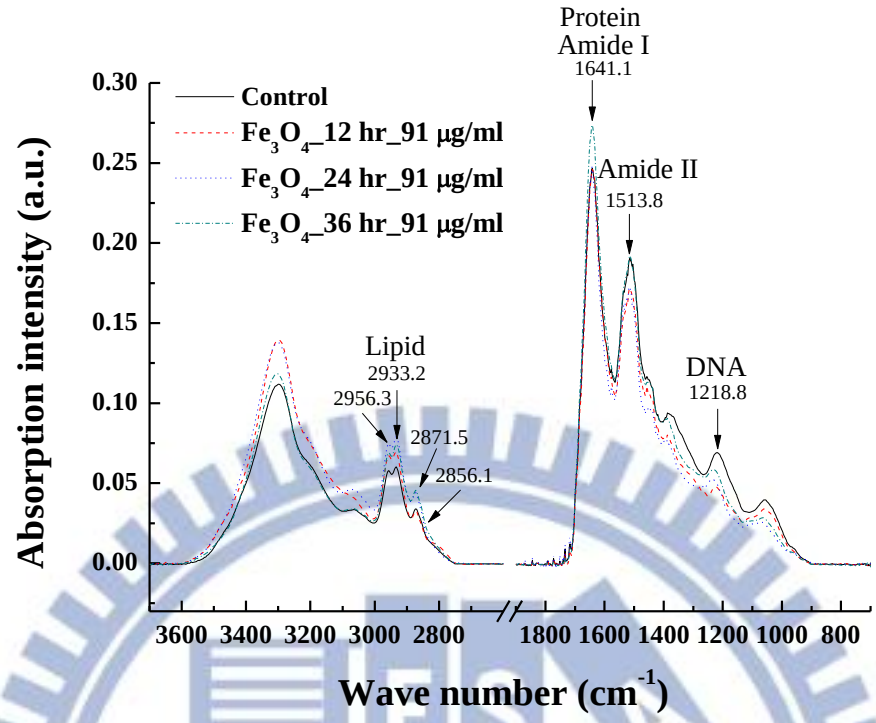

Figure 4.11 The spectra of time effect of Fe_3O_4 MNPs to A549 cells at the applied concentration 91 μ g/ml.

However, the magnification shown in Figure 4.12, which is the magnification of each primary regions, lipid, protein, and DNA regions from Fig. 4.10 shows that no peak shift occurs in lipid and protein regions, while a little peak shift in the asymmetric PO_2^- region is observed under various MNPs treatment times. The spectra of DNA region display the peaks at 1218.8 cm^{-1}, 1224.6 cm^{-1}, 1236.1 cm^{-1} and 1232.3 cm^{-1} corresponding to the control sample, and A549 cells treated with MNPs for 12, 24 and 36 hr, respectively. The longer Fe_3O_4 MNPs treatment time is, the higher wave number the peak position shifts towards. This indicates that DNA structures are influenced by Fe_3O_4 MNPs and this change becomes more dramatic with MNPs

treatment times. That the asymmetric PO_2^- peak shifts toward higher wave number indicates that it requires more energy to excite the ground state of asymmetric PO_2^- stretching vibration mode into its exited state. This suggests that the chemical environment of PO_2^- group in A549 cells is changed when A549 cells are exposed to Fe_3O_4 MNPs. Since the asymmetric PO_2^- peak primarily dominates in DNA, this result therefore indicates that DNA structure is changed into disordered structure by the interaction of A549 cells and Fe_3O_4 MNPs. Besides, both signatures of cell death are not observed, first is no -C=O ester peak around 1740 cm^{-1} and second is no peak shift in protein region[66]. Hence, this result shows that Fe_3O_4 MNPs-treated A549 cells are not dead, despite of DNA structure change. Also, from the increase of the formazan absorption intensity, it is most likely that as a consequence of restoring its DNA structure, the cell cycle life of A549 cells is prolonged, not the decrease in A549 cell number.

Although there is no peak shift in lipid and protein regions, that is, no dramatic structure change in lipid and protein, however, the ratio of lipid to protein increases with MNPs treatment time (Figure 4.13). The amount of lipid is calculated from the absorption area from 2800 to 3000 cm^{-1}, while that of protein is calculated from the absorption area from 1450 to 1750 cm^{-1}. The climb of the lipid/ protein ratio means the amount of proteins relatively declines, while that of lipids relatively increases when A549 cells are treated with Fe_3O_4 MNPs. There are several literatures [67-68]describing that the increase of the lipid/ protein ratio is associated with the onset of apoptosis, but the lipid/ protein ratio they used is base on the peak height of symmetric methylene CH_2 stretching vibration mode around 2852 cm^{-1}, which is expressed as lipid, over the peak height of CH_3, which is presented as protein around

1400 cm^{-1}. However, in our case, the height of symmetric CH_2 peak is not obvious; instead, the area of absorption of lipid and that of protein are used to calculate the lipid/protein ratio. Therefore, the increase in the lipid/protein ratio indicates that apoptosis process maybe begins when A549 cells are treated with MNPs concentration 91 μg/ml for increasing MNPs treatment times. Despite of the increase in the lipid/protein ratio, as discussed above, there is no signature of cell death observed. Besides, it seems that the lipid/protein ratio is decreased at 36 hr. Hence, this DNA structure change may be reversible, that is, DNA structure change can be recovered when A549 cells are treated at the applied concentration at 91 μg/ml. Consequently, no A549 cells die out, but instead their cell cycle life is prolonged.

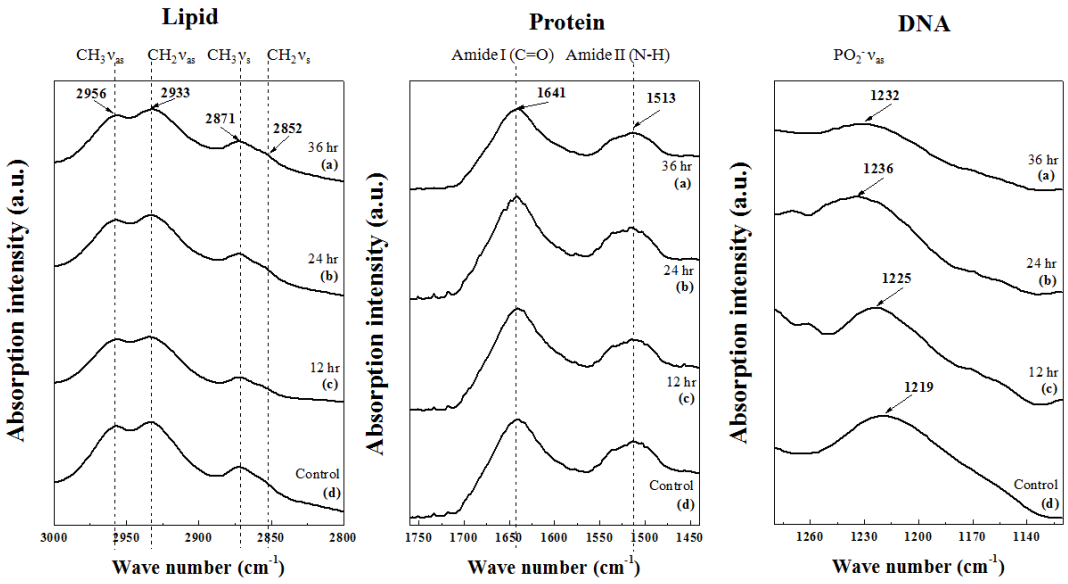

Figure 4.12 Absorption peak positions of lipid, protein and DNA regions under different Fe_3O_4 MNPs treatment times at the applied concentration 91 μg/ml.

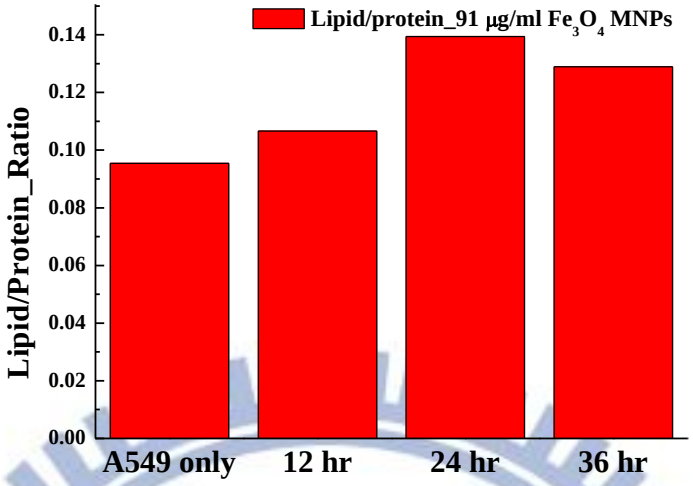

Figure 4.13 The ratio of lipid to protein with different Fe_3O_4 MNPs treatment times at the applied concentration 91 μ g/ml.

4.3.1.2 Concentration Effect

Figure 4.14 shows the normalized spectra change of A549 cells treated with different Fe_3O_4 MNPs concentrations 11 and 91 μ g/ml for 36 hr. There is also no peak shift in lipids and proteins regions, shown in Figure 4.15. When A549 cells are exposed to different Fe_3O_4 MNPs concentrations under 36hr treatment time, a peak shift at the asymmetric PO_2^- stretching vibration mode is toward higher wave number 1232.3 cm^{-1}, compared with the control group with peak position at 1218.8 cm^{-1} (Fig. 4.15). This peak shift is independent of Fe_3O_4 MNPs concentration at 36 hr treatment time. This result suggests that under different Fe_3O_4 MNPs concentrations 11 and 91 μ g/ml at 36 hr treatment time, DNA structure change is the same. This DNA structure change does not cause A549 cells dead, and may be recovered, because no

signatures of cell death are observed, that is, no peak shift in protein region and no –C=O ester peak are observed. Although no structure changes of proteins and lipids are observed, the lipid/protein ratio remains the same for different MNPs concentrations, but higher than that for the control group (Fig. 4.16). This means that A549 cells treated with Fe_3O_4 MNPs experience the same intracellular chemical change after 36 hr treatment time no matter what MNPs concentration is between 11 to 91 μ g/ml. This result is in agreement with the same cell viability of A549 cells treated with Fe_3O_4 MNPs concentration 11 and 91 μ g/ml for 36 hr (Fig. 4.9).

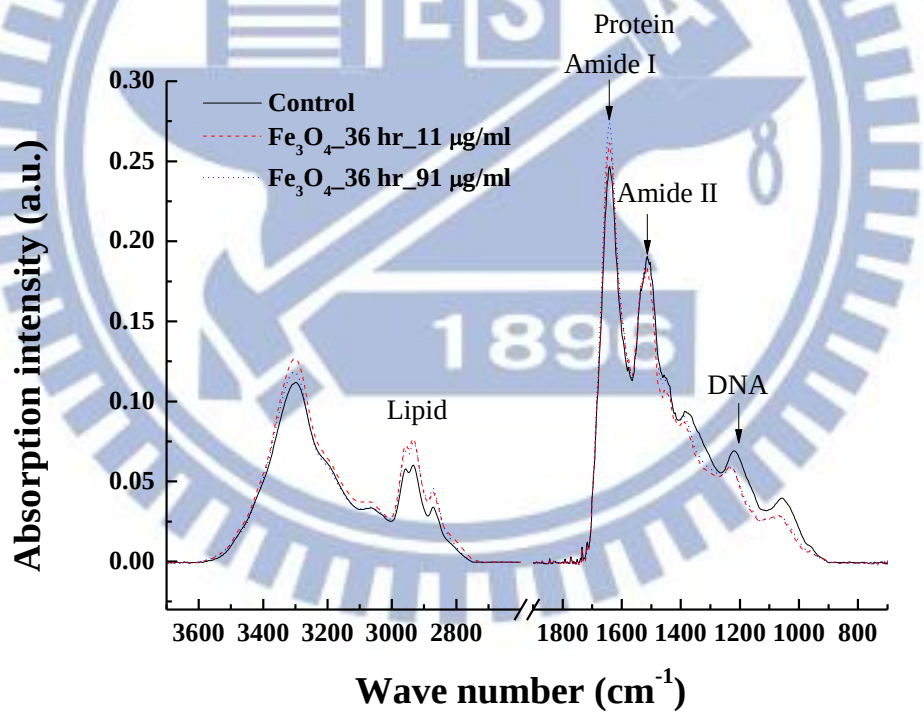

Figure 4.14 The spectra of concentration effect of Fe_3O_4 MNPs to A549 cells for 36 hr treatment time.

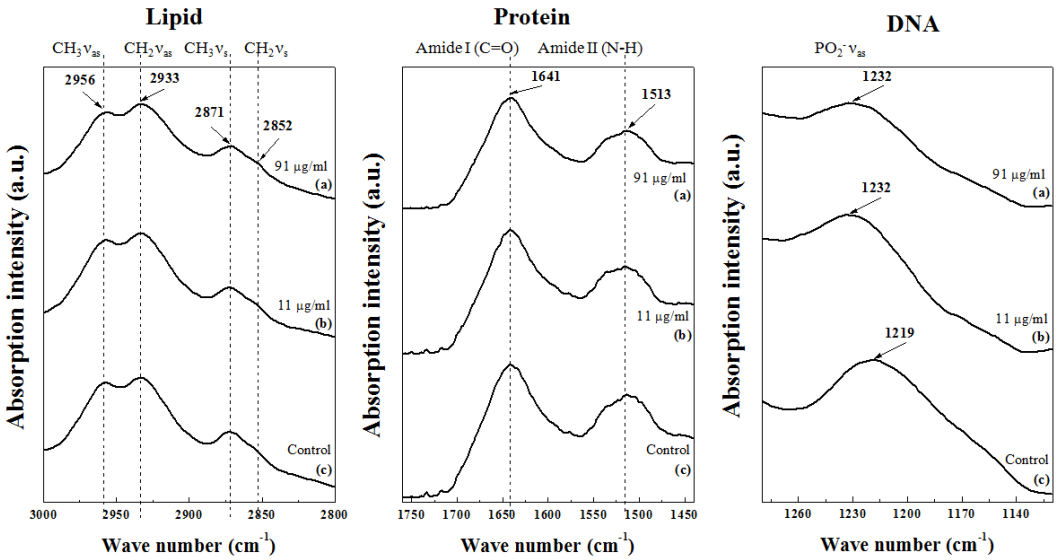

Figure 4.15 Absorption peak positions of lipid, protein and DNA regions under different Fe_3O_4 MNPs concentrations for 36hr treatment time.

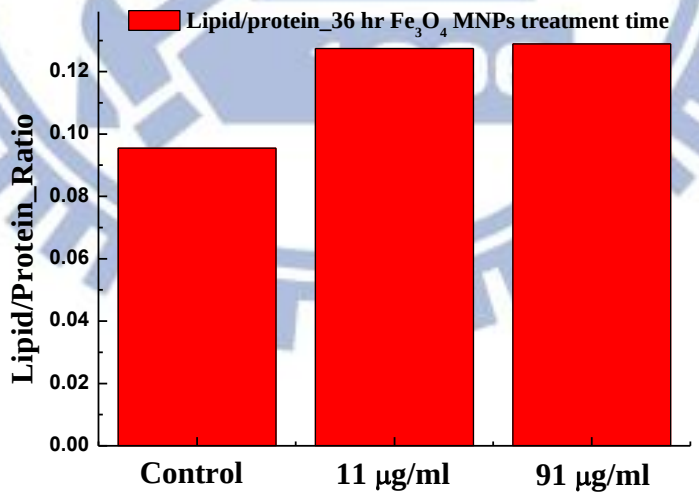

Figure 4.16 The ratio of lipid to protein with different Fe_3O_4 MNPs concentrations for 36 hr treatment time.

4.3.2 A549 treated with Fe_3O_4@SiO_2

4.3.2.1 Treatment Time Effect

Figure 4.17 shows the normalized spectra of A549 cells treated with Fe_3O_4@SiO_2 MNPs concentration 91 μ g/ml for different MNPs treatment times, 12, 24 and 36 hr. There are only subtle differences between each other. The bands assignment is the same as that in Figure 4.11. It seems that no dramatic changes in spectra of A549 cells when A549 cells are exposed to these two different nanomaterials, Fe_3O_4 MNPs and Fe_3O_4@SiO_2 MNPs.

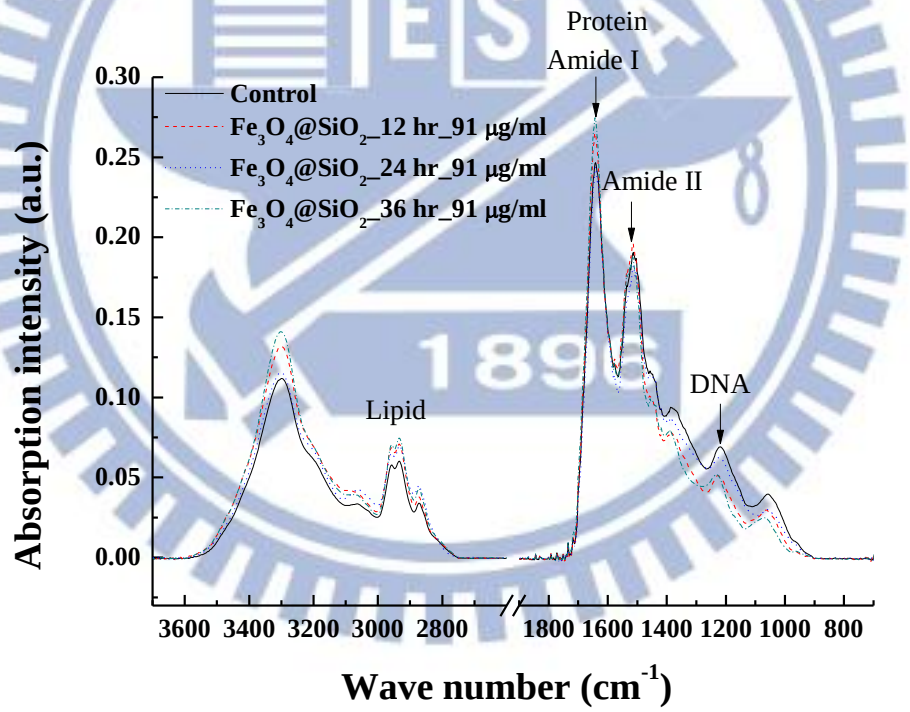

Figure 4.17 The spectra of time effect of Fe_3O_4@SiO_2 MNPs to A549 cells at the applied concentration 91 μ g/ml.

Figure 4.18 exhibits the magnification of primary regions (lipids, proteins and DNA) of the control group and A549 cells treated with Fe_3O_4@SiO_2 MNPs concentration 91 μg/ml for different times. There is no lipid and protein peak shift. However, it shows that a little peak position shift for different MNPs treatment time. The peak positions are at 1218.8, 1226.5, 1222.6 and 1232.3 cm^{-1} for the control group and the samples treated with MNPs for 12, 24, and 36 hr, respectively. The trends of the asymmetric stretching mode of PO_2^- peak position are the same for A549 cells treated with Fe_3O_4 MNPs and Fe_3O_4@SiO_2 MNPs under different times. This suggests that DNA structures change affected by Fe_3O_4 MNPs and Fe_3O_4@SiO_2 MNPs are clearly seen. Besides, no protein peak shift and no –C=O ester peak are observed. These results indicate that A549 cells are not dead when treated with MNPs for these time periods. The lipid/protein ratio is shown in Figure 4.19. This ratio increases during 24 hr MNPs treatment time, but it shows that at 36 hr MNPs treatment time, this ratio decreases a little. This may indicate that the apoptosis is not onset due to the decrease of the lipid/protein ratio after 24 hr.

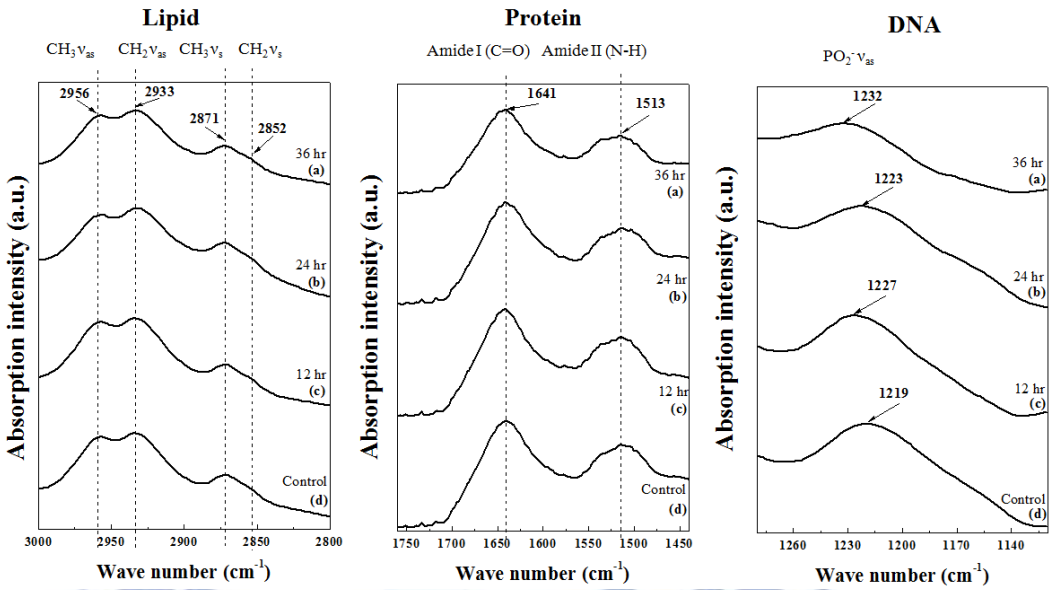

Figure 4.18 Absorption peak positions of lipid, protein and DNA regions under different Fe_3O_4@SiO_2 MNPs treatment times at the applied concentration 91 μ g/ml.

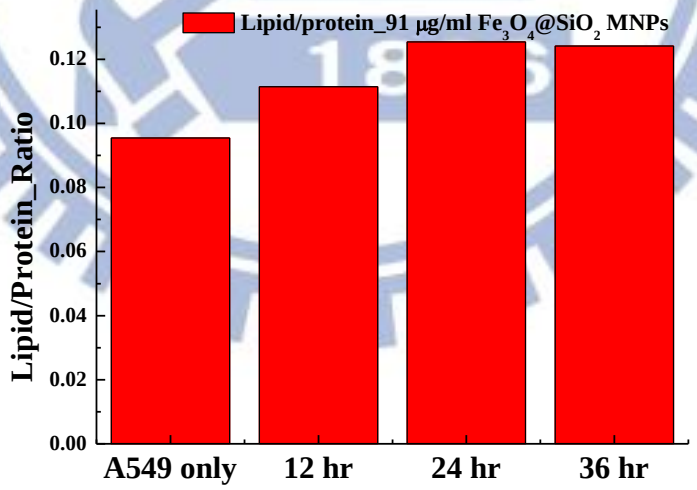

Figure 4.19 The ratio of lipid to protein with different Fe_3O_4@SiO_2 MNPs treatment times at the applied concentration 91 μ g/ml.

4.3.2.2 Concentration Effect

The normalized spectra of A549 cells treated with different Fe_3O_4@SiO_2 MNPs concentrations for 36 hr are shown in Figure 4.20. There is no obvious difference between the spectra of A549 cells treated with different Fe_3O_4@SiO_2 MNPs concentrations.

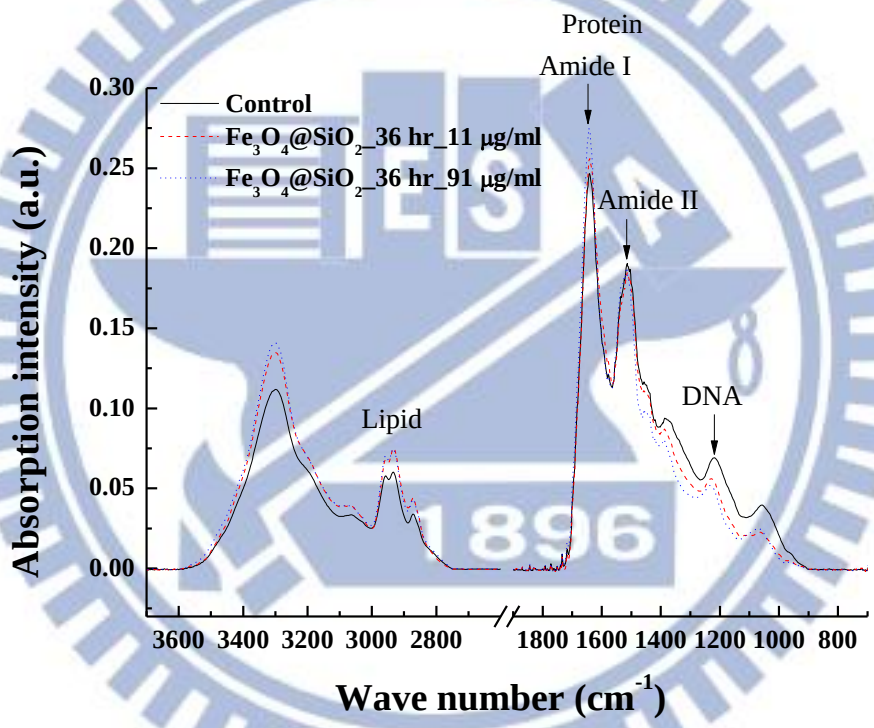

Figure 4.20 The spectra of concentration effect of Fe_3O_4@SiO_2 MNPs to A549 cells for 36 hr treatment time.

At the first glance of Figure 4.20, although it shows no apparent change in the

spectra, the fact is that there is a peak shift at the asymmetric stretching vibration mode of PO_2^- (Fig. 4.21). The peak position is at 1232.3 cm^{-1} for both A549 cells treated with 11 and 91 μ g/ml Fe_3O_4@SiO_2 MNPs, similar to the results of A549 cells treated with 11 and 91 μ g/ml Fe_3O_4 MNPs. This indicates that DNA structure change is indirectly related to the composition of nanomaterials exposing to A549 cells in our case. The DNA structure change in A549 cells is a cellular response when A549 cells are exposed to outside triggers. This is accordant with the cell viability result that both cell viabilities of A549 cells treated with Fe_3O_4 MNPs and Fe_3O_4@SiO_2 MNPs are almost the same. Besides, the DNA structure change may be reversible because of the decrease of the lipid/protein ratio after 24 hr.

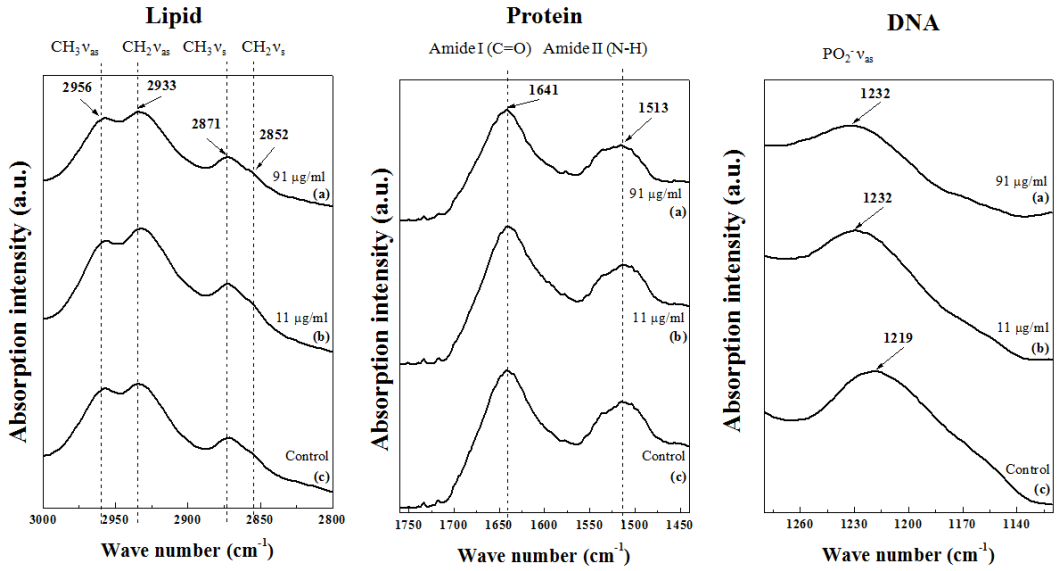

Figure 4.21 Absorption peak positions of lipid, protein and DNA regions under different Fe_3O_4@SiO_2 MNPs concentrations for 36 hr treatment time.

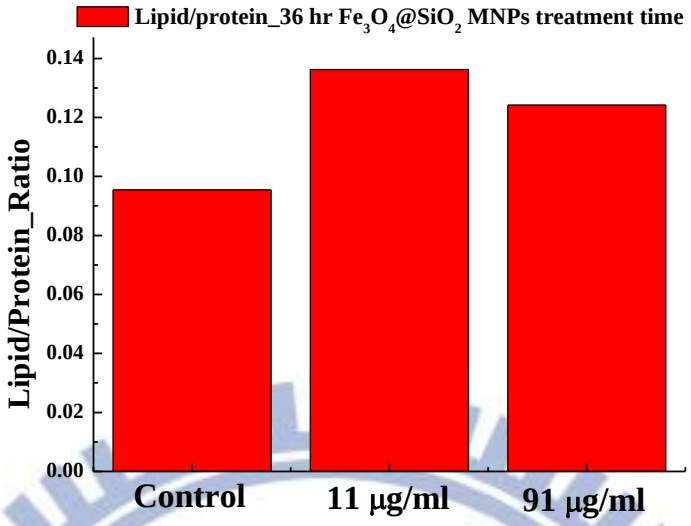

Figure 4.22 The ratio of lipid to protein with different Fe_3O_4@SiO_2 MNPs concentrations for 36 hr treatment time.

4.3.3 SRIR Images of A549 cells treated with Fe_3O_4 MNPs

Figure 4.23 shows the chemical mapping of the control group (Fig. 4.23(a))and A549 cells treated with different Fe_3O_4 MNPs concentrations 11 and 91 μ g/ml for 36 hr (Fig. 4.23(b) and (d), respectively)and with Fe_3O_4 MNPs concentration 91 μ g/ml for different treatment times 12 and 36 hr (Fig. 4.23(c) and (d)). The lipid distribution map is associated to the C-H stretching bands from 2800 to 3000 cm^{-1}.The protein distribution map results from the Amide I and Amide II bands integration from 1470 to 1750 cm^{-1}. The DNA distribution map is based on the integration of the asymmetric stretching vibration mode of PO_2^- from 1180 to 1260 cm^{-1}. The spectra were measured by an aperture 15×15 μm^2 with a step size 10 μ m. The spectral resolution is 4 cm^{-1} and 256 scans for spectrum of each position were accumulated.

In Figure 4.23(a), the size of an A549 cell is around 20 to 30 μm, and DNA and proteins are localized in the almost the same small region where is defined as cell nucleus. Figure 4.23(b) displays the chemical mapping of lipids, proteins and DNA when A549 cells are treated with 11 μg/ml Fe_3O_4 MNPs for 36 hr. It is observed that in the DNA chemical mapping of 36hr-MNPs-treated A549 cells, there is a small signal appearing at the background out of the cell, and this indicates that the intensity of DNA declines, compared with control group. Besides, there is a small change in the lipid distribution, but this maybe also results from different states of cells.

In order to understand the chemical composition distribution of A549 cells treated with different Fe_3O_4 MNPs concentrations at a given time, the chemical mapping of A549 cells treated with the concentration 91 μg/ml for 36 hr treatment time were measured as shown in Figure 4.23(d). Compared with Figure 4.23(b), the DNA distribution and the protein distribution of A549 cells treated with the concentration 91 μg/ml are much widespread than those of A549 cells treated with the lower concentration 11 μg/ml. This indicates that the distributions of DNA and proteins are severely affected by Fe_3O_4 MNPs concentration 91 μg/ml. Also, for DNA chemical mapping, the intensity of background outside the A549 cell treated at the concentration 91 μg/ml becomes higher than that of the cell shown in Figure 4.23(b). The higher the intensity of background outside the A549 cell is, the lower the DNA concentration in the A549 cell is. Hence, after the A549 cell was treated with Fe_3O_4 MNPs concentration 91 μg/ml, the DNA concentration in the cell became lower, compared with the control group and A549 treated with MNPs concentration 11 μg/ml. This result indicates that besides DNA structure change, the DNA concentration is lower when A549 cells are treated with MNPs.

For the time effect of Fe_3O_4 MNPs to A549 cells, it seems that the background signal in the DNA chemical mapping of A549 cells treated with 91 μg/ml for 12 hr (Fig. 4.23(c)) is less than that of A546 cells treated with MNPs for 36 hr. This indicates that the DNA concentration is much lower for A549 cells treated with MNPs for 36 hr.

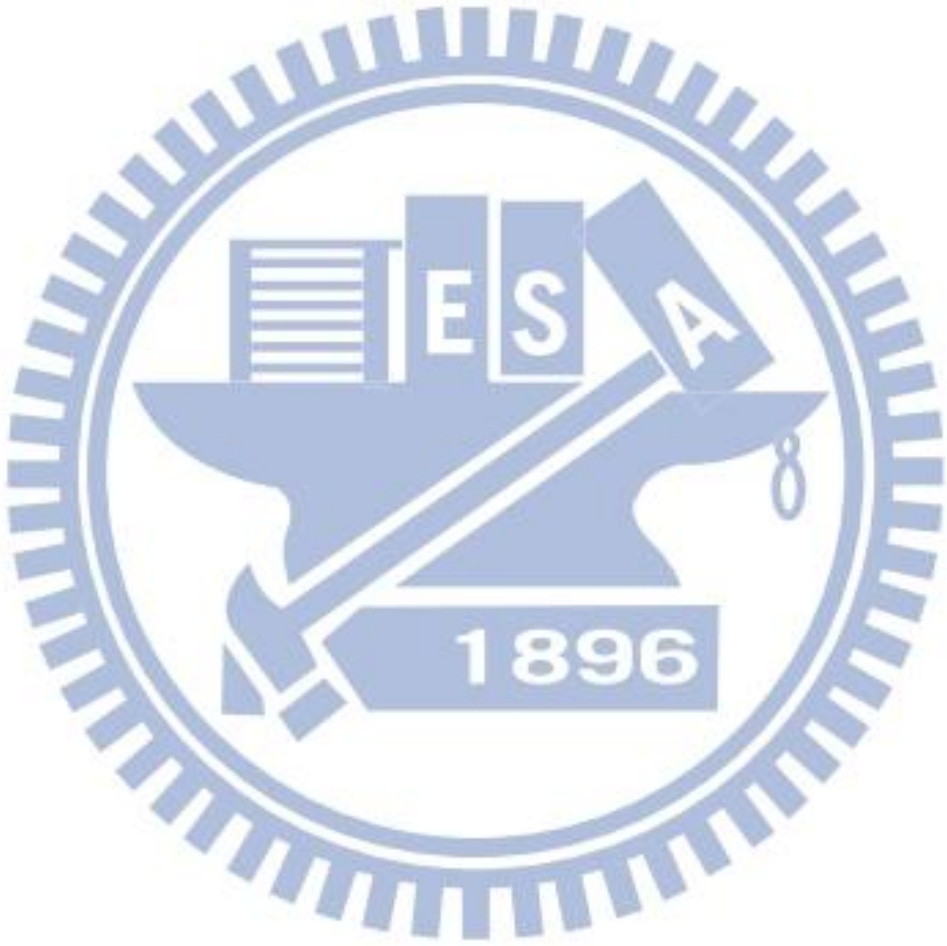

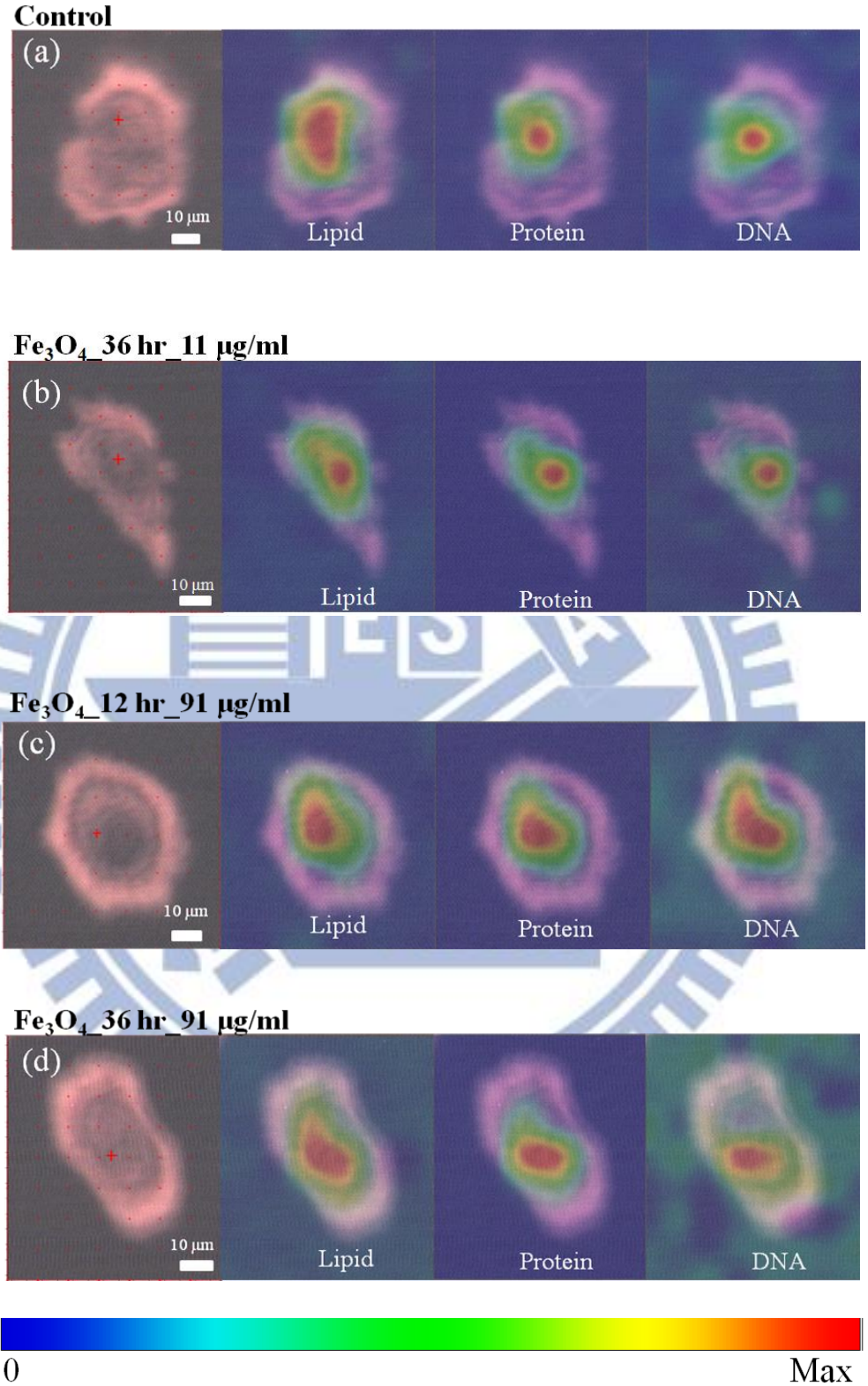

Figure 4.23 The microscopic image of A549 cells and the chemical mappings with different constituents of A549 cells treated with different Fe_3O_4 MNPs concentrations for different MNPs treatment times.

In order to know whether Fe_3O_4 MNPs affect different parts in cells or not, spectra of different locations in A549 cells are extracted, shown in Figure 4.24, 4.25, 4.26 and 4.27 for the control group A549 cell, the A549 cell treated at the applied Fe_3O_4 MNPs concentration 11 μg/ml for 36 hr, the A549 cell treated at the applied Fe_3O_4 MNPs concentration 91 μg/ml for 12 hr, and the A549 cell treated at the applied Fe_3O_4 MNPs concentration 91 μg/ml for 36 hr, respectively. The locations

It can be observed that compared with each different location, there is no primary peak shift in lipid, protein and DNA regions for different locations in A549 cells under different conditions. Therefore, this indicates after A549 cells are treated with 91 μg/ml for 12 hr, the chemical structure changes are completely the same at different locations, which suggests that this structure change induced by the interaction between A549 cell and MNPs is less than 12 hr. However, this does not mean that there is no primary peak shift for A549 cells under different conditions. Just as above-discussed, DNA structures are affected under different conditions.

Although there is no dramatic structure change in different locations, the relative amounts of biological components in different locations in A549 cells are various. It is observed that at the region 1 the amount of proteins is relatively larger than those of lipids and DNA for all situations. When location is far than the nucleus region (region 1), the amount of protein becomes relative smaller, while that of lipid is relatively larger at the regions 2 and 3. That is, the relative amount of lipids, compared with that of proteins, is larger at far nucleus region. Most proteins are localized around and at the nucleus region. Because when cells are interacting with outer triggers or ligands, cells should do some cellular responses, based on their blue print, DNA, therefore, this result may be explained by the fact that in order to magnify signals to DNA, the

distribution of proteins should take this form to respond rapidly.

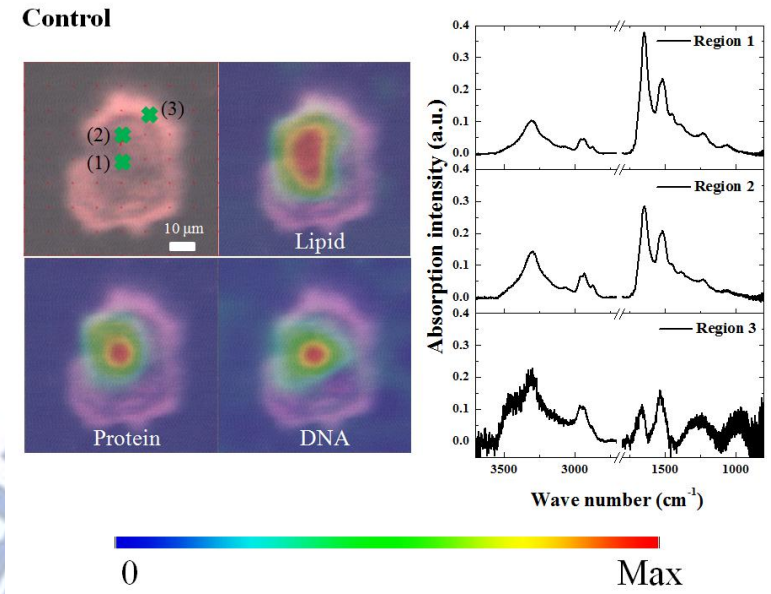

Figure 4.24 The spectra of different locations in the control group A549 cell.

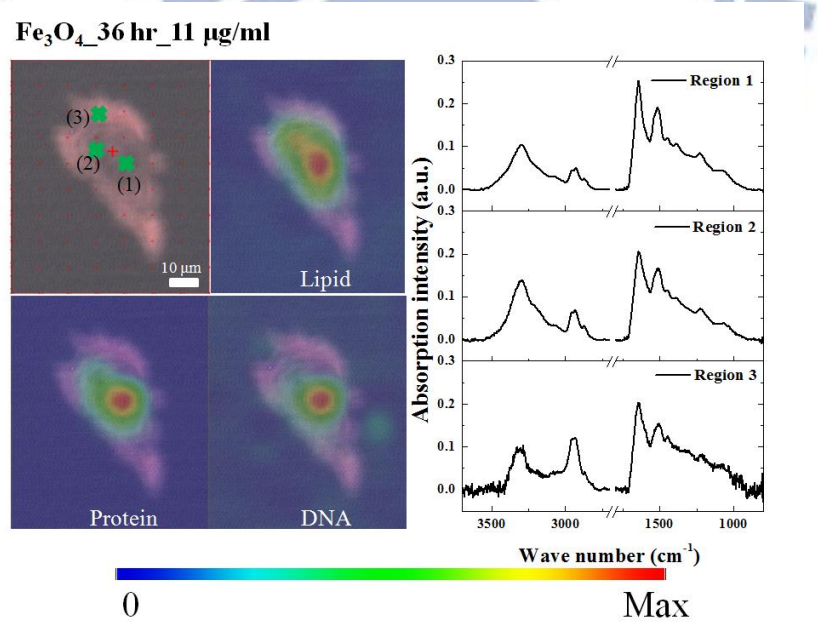

Figure 4.25 The spectra of different locations in the A549 cell treated with Fe_3O_4 MNPs concentration 11 μg/ml for 36 hr.

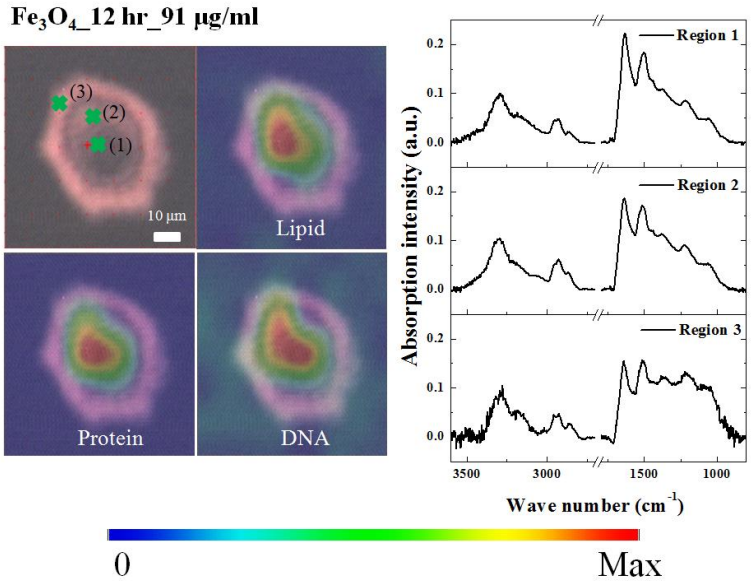

Figure 4.26 The spectra of different locations in the A549 cell treated with Fe_3O_4 MNPs concentration 91 μg/ml for 12 hr.

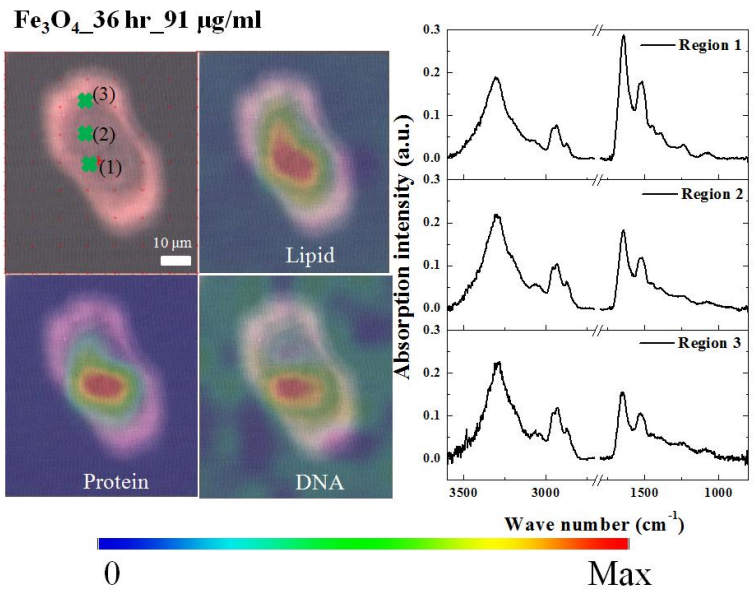

Figure 4.27 The spectra of different locations in the A549 cell treated with Fe_3O_4 MNPs concentration 91 μg/ml for 36 hr.

Chapter 5 Conclusions and Future Works

As-prepared Fe_3O_4 MNPs and Fe_3O_4@SiO_2 MNPs are successfully synthesized by coprecipitation method and Stöber method, respectively. The cytotoxicity of these MNPs in A549 lung cancer cells is obtained by MTT assay, and the results show that both Fe_3O_4 MNPs and Fe_3O_4@SiO_2 MNPs exhibit almost no toxicity to A549 cells at applied concentrations from 0 to 91 μg/ml for 12 hr treatment time, while the cytotoxicity of both MNPs emerges after 24 hr MNPs treatment time even at the lowest concentration 6 μg/ml at which the cell viability is around 80 % in this study. This result shows that cytotoxicity is time- and concentration- dependent. By SRIR spectrum measurement, DNA structures are affected by MNPs and become more dramatic with MNPs treatment times at the applied concentration 91 μg/ml, but no signatures of cell death are observed. Besides, the change of DNA structures maintain the same at two applied concentrations 11 and 91 μg/ml for 36 hr treatment time. When A549 cells are exposed to Fe_3O_4 MNPs and Fe_3O_4@SiO_2 MNPs, the DNA structure change almost the same for each condition, this indicates that this cellular response is a characteristic of A549 cell upon outer trigger. No dramatic lipid and protein structures are observed, but the lipid/protein ratio increases during 24 hr MNPs treatment time but decreases at 36 hr at the applied MNPs concentration 91 μ g/ml, while this ratio remains almost the same at different MNPs treatment concentration for 36 hr. By SRIRM, for A549 cells treated with Fe_3O_4 MNPs, the concentration of DNA decreases; however, DNA remains mostly at the nucleus. Also, the relatively amount of proteins is larger at and around the nucleus, while that of lipids is relative larger at the far-nucleus region. In summary, we demonstrate a

different technique, SRIRM, to observe the chemical constituent change and the chemical composition distribution when cells are exposed to nanomaterials.

In the future work, in order to understand the relationship between the change of DNA structure and MNPs, XAS will be conducted to study the change of oxidation state of MNPs when these MNPs interact with A549 cells for different MNPs treatment times. Besides, in order to know whether MNPs enter into A549 cells, instead of TEM, Transmission X-ray Microscopy (TXM) will be performed because samples can be in a more native state. Or even Soft X-ray transmission microscopy can be carried out to visualize the distribution of organic components and MNPs in cells. The amount of MNPs cellular uptake will be measured by ICP-MS.

Reference

[1] Lu AH, Salabas EL, Schüth F. Magnetic Nanoparticles: Synthesis, Protection, Functionalization, and Application. Angewandte Chemie International Edition. 2007;46(8):1222-44.

[2] Zhao YS, Fu H, Peng A, Ma Y, Liao Q, Yao J. Construction and Optoelectronic Properties of Organic One-Dimensional Nanostructures. Accounts of Chemical Research. 2009;43(3):409-18.

[3] Ray PC. Size and Shape Dependent Second Order Nonlinear Optical Properties of Nanomaterials and its Application in Biological and Chemical Sensing. Chemical Reviews. 2010;110(9):5332.

[4] Zhang G, Li B. Impacts of Doping on Thermal and Thermoelectric Properties of Nanomaterials. Nanoscale. 2010;2(7):1058-68.

[5] Alayoglu S, Nilekar AU, Mavrikakis M, Eichhorn B. Ru–Pt Core–Shell Nanoparticles for Preferential Oxidation of Carbon Monoxide in Hydrogen. Nature Materials. 2008;7(4):333-8.

[6] Xia T, Kovochich M, Brant J, Hotze M, Sempf J, Oberley T, et al. Comparison of the Abilities of Ambient and Manufactured Nanoparticles to Induce Cellular Toxicity According to an Oxidative Stress Paradigm. Nano Letters. 2006;6(8):1794-807.

[7] Limbach LK, Wick P, Manser P, Robert N, Bruinink A, Stark WJ. Exposure of Engineered Nanoparticles to Human Lung Epithelial Cells: Influence of Chemical Composition and Catalytic Activity on Oxidative Stress. Environmental Science & Technology. 2007;41(11):4158-63.

[8] Könczöl M, Ebeling S, Goldenberg E, Treude F, Gminski R, Gieré R, et al. Cytotoxicity and Genotoxicity of Size-Fractionated Iron Oxide (magnetite) in A549 Human Lung Epithelial Cells: Role of ROS, JNK, and NF-κB. Chem Res Toxicol. 2011;24(9):1460-75.

[9] Ye Y, Liu J, Xu J, Sun L, Chen M, Lan M. Nano-SiO_2 Induces Apoptosis Via Activation of p53 and Bax Mediated by Oxidative Stress in Human Hepatic Cell Line. Toxicology in Vitro. 2010;24(3):751-8.

[10] Lin W, Huang Y, Zhou XD, Ma Y. In Vitro Toxicity of Silica Nanoparticles in Human Lung Cancer Cells. Toxicology and Applied Pharmacology. 2006;217(3):252-9.

[11] Hengartner MO. The Biochemistry of Apoptosis. Nature. 2000;407(6805):770-6.

[12] Zhao J, Bowman L, Zhang X, Vallyathan V, Young SH, Castranova V, et al. Titanium Dioxide (TiO2) Nanoparticles Induce JB6 Cell Apoptosis through Activation of the Caspase-8/Bid and Mitochondrial Pathways. Journal of Toxicology and Environmental Health, Part A. 2009;72(19):1141-9.

[13] Ramesh V, Ravichandran P, Copeland CL, Gopikrishnan R, Biradar S, Goornavar V, et al. Magnetite Induces Oxidative Stress and Apoptosis in Lung Epithelial Cells. Molecular and Cellular Biochemistry. 2012:1-10.

[14] Khan MI, Mohammad A, Patil G, Naqvi S, Chauhan L, Ahmad I. Induction of ROS, Mitochondrial Damage and Autophagy in Lung Epithelial Cancer Cells by Iron Oxide Nanoparticles. Biomaterials. 2012;33(5):1477-88.

[15] Nel A, Xia T, Mädler L, Li N. Toxic Potential of Materials at the Nanolevel. Science. 2006;311(5761):622-7.

[16] Li N, Sioutas C, Cho A, Schmitz D, Misra C, Sempf J, et al. Ultrafine Particulate Pollutants Induce Oxidative Stress and Mitochondrial Damage. Environmental

Health Perspectives. 2003;111(4):455.

[17] Fubini B, Hubbard A. Reactive Oxygen Species (ROS) and Reactive Nitrogen Species (RNS) Generation by Silica in Inflammation and Fibrosis. Free Radical Biology and Medicine. 2003;34(12):1507-16.

[18] Auffan M, Rose J, Wiesner MR, Bottero JY. Chemical Stability of Metallic Nanoparticles: A Parameter Controlling Their Potential Cellular Toxicity in Vitro. Environmental Pollution. 2009;157(4):1127-33.

[19] Cao SW, Zhu YJ, Ma MY, Li L, Zhang L. Hierarchically Nanostructured Magnetic Hollow Spheres of Fe_3O_4 and γ-Fe_2O_3: Preparation and Potential Application in Drug Delivery. The Journal of Physical Chemistry C. 2008;112(6):1851-6.

[20] Pankhurst QA, Connolly J, Jones S, Dobson J. Applications of Magnetic Nanoparticles in Biomedicine. Journal of Physics D: Applied Physics. 2003;36:R167.

[21] Liong M, Angelos S, Choi E, Patel K, Stoddart JF, Zink JI. Mesostructured Multifunctional Nanoparticles for Imaging and Drug Delivery. J Mater Chem. 2009;19(35):6251-7.

[22] Zhang J, Sun W, Bergman L, Rosenholm JM, Lindén M, Wu G, et al. Magnetic Mesoporous Silica Nanospheres as DNA/Drug Carrier. Materials Letters. 2012;67(1):379-82.

[23] Shao M, Ning F, Zhao J, Wei M, Evans DG, Duan X. Preparation of Fe_3O_4@ SiO_2@ Layered Double Hydroxide Core–Shell Microspheres for Magnetic Separation of Proteins. Journal of the American Chemical Society. 2012;134(2):1071-7.

[24] Yang L, Ren X, Tang F, Zhang L. A Practical Glucose Biosensor Based on Fe_3O_4

Nanoparticles and Chitosan/Nafion Composite Film. Biosensors and Bioelectronics. 2009;25(4):889-95.

[25] Qiu J, Peng H, Liang R. Ferrocene-Modified Fe_3O_4@ SiO_2 Magnetic Nanoparticles as Building Blocks for Construction of Reagentless Enzyme-based Biosensors. Electrochemistry Communications. 2007;9(11):2734-8.

[26] Cheng Y, Liu Y, Huang J, Li K, Xian Y, Zhang W, et al. Amperometric Tyrosinase Biosensor Based on Fe_3O_4 Nanoparticles-Coated Carbon Nanotubes Nanocomposite for Rapid Detection of Coliforms. Electrochimica Acta. 2009;54(9):2588-94.

[27] Loh KS, Lee YH, Musa A, Salmah AA, Zamri I. Use of Fe_3O_4 Nanoparticles for Enhancement of Biosensor Response to the Herbicide 2, 4-dichlorophenoxyacetic Acid. Sensors. 2008;8(9):5775-91.

[28] Jeng HA, Swanson J. Toxicity of Metal Oxide Nanoparticles in Mammalian Cells. Journal of Environmental Science and Health Part A. 2006;41(12):2699-711.

[29] Karlsson HL, Cronholm P, Gustafsson J, Möller L. Copper Oxide Nanoparticles Are Highly Toxic: A Comparison between Metal Oxide Nanoparticles and Carbon Nanotubes. Chemical Research in Toxicology. 2008;21(9):1726-32.

[30] Karlsson HL, Gustafsson J, Cronholm P. Size-Dependent Toxicity of Metal Oxide Particles--A Comparison between Nano-and Micrometer Size. Toxicology Letters. 2009;188(2):112-8.

[31] Singh N, Jenkins GJS, Nelson BC, Marquis BJ, Maffeis TGG, Brown AP, et al. The Role of Iron Redox State in the Genotoxicity of Ultrafine Superparamagnetic Iron Oxide Nanoparticles. Biomaterials. 2012;33(1):163-70.

[32] Chang JS, Chang KLB, Hwang DF, Kong ZL. In Vitro Cytotoxicitiy of Silica Nanoparticles at High Concentrations Strongly Depends on the Metabolic

Activity Type of The Cell Line. Environmental Science & Technology. 2007;41(6):2064-8.

[33] Mbeh D, França R, Merhi Y, Zhang X, Veres T, Sacher E, et al. In Vitro Biocompatibility Assessment of Functionalized Magnetite Nanoparticles: Biological and Cytotoxicological Effects. Journal of Biomedical Materials Research Part A. 2012;100A(6):1637-46.

[34] Mahmoudi M, Laurent S, Shokrgozar MA, Hosseinkhani M. Toxicity Evaluations of Superparamagnetic Iron Oxide Nanoparticles: Cell Vision Versus Physicochemical Properties of Nanoparticles. Acs Nano. 2011;5(9):7263-76.

[35] Cullity BD, Stock SR. Elements of X-ray Diffraction: Prentice hall Upper Saddle River, NJ; 2001.

[36] Hüfner S. Photoelectron Spectroscopy: Principles and Applications: Springer Verlag; 2003.

[37] Sayers DE, Stern EA, Lytle FW. New Technique for Investigating Noncrystalline Structures: Fourier Analysis of the Extended X-Ray—Absorption Fine Structure. Physical Review Letters. 1971;27(18):1204-7.

[38] Hwang BJ, Sarma LS, Chen JM, Chen CH, Shih SC, Wang GR, et al. Structural Models and Atomic Distribution of Bimetallic Nanoparticles as Investigated by X-ray Absorption Spectroscopy. Journal of the American Chemical Society. 2005;127(31):11140-5.

[39] Dumas P, Miller L. Biological and Biomedical Applications of Synchrotron Infrared Microspectroscopy. Journal of Biological Physics. 2003;29(2):201-18.

[40] Miller LM, Dumas P. Chemical Imaging of Biological Tissue with Synchrotron Infrared Light. Biochimica et Biophysica Acta (BBA)-Biomembranes. 2006;1758(7):846-57.

[41] Dumas P, Sockalingum GD, Sulé-Suso J. Adding Synchrotron Radiation to Infrared Microspectroscopy: What's New in Biomedical Applications? Trends in Biotechnology. 2007;25(1):40-4.

[42] Darzynkiewicz Z, Li X, Gong J. Assays of Cell Viability: Discrimination of Cells Dying by Apoptosis. Methods in Cell Biology, Vol 41. 1994;41:15-38.

[43] Koopman G, Reutelingsperger C, Kuijten G, Keehnen R, Pals S, Van Oers M. Annexin V for Flow Cytometric Detection of Phosphatidylserine Expression on B Cells Undergoing Apoptosis. Blood. 1994;84(5):1415-20.

[44] Strober W. Trypan Blue Exclusion Test of Cell Viability. Current Protocols in Immunology. 2001: Appendix 3B.

[45] Chan LL, Wilkinson AR, Paradis BD, Lai N. Rapid Image-based Cytometry for Comparison of Fluorescent Viability Staining Methods. Journal of Fluorescence. 2012:1-11.

[46] Mozes E, Hunya A, Posa A, Penke B, Datki Z. A Novel Method for the Rapid Determination of Beta-amyloid Toxicity on Acute Hippocampal Slices Using MTT and LDH Assays. Brain Research Bulletin. 2012;87(6):521-5.

[47] Liu Y, Peterson DA, Kimura H, Schubert D. Mechanism of Cellular 3-(4, 5-dimethylthiazol-2-yl)-2, 5-diphenyltetrazolium Bromide (MTT) Reduction. Journal of Neurochemistry. 1997;69(2):581-93.

[48] Marques EP, Zhang J, Tse YH, Metcalfe RA, Pietro WJ, Lever A. Surface Electrochemistry of 3-(4, 5-dimethylthiazol-2-yl)-2, 5-diphenyl-2H-tetrazolium Bromide ([MTT] Br) Adsorbed on a Graphite Electrode. Journal of Electroanalytical Chemistry. 1995;395(1):133-42.

[49] Cheng FY, Su CH, Yang YS, Yeh CS, Tsai CY, Wu CL, et al. Characterization of Aqueous Dispersions of Fe_3O_4 Nanoparticles and Their Biomedical Applications.

Biomaterials. 2005;26(7):729-38.

[50] Santra S, Zhang P, Wang K, Tapec R, Tan W. Conjugation of Biomolecules with Luminophore-doped Silica Nanoparticles for Photostable Biomarkers. Analytical Chemistry. 2001;73(20):4988-93.

[51] NSRRC website http://140.110.203.42/EFD.php?num=227.

[52] Ravel B, Newville M. ATHENA, ARTEMIS, HEPHAESTUS: Data Analysis for X-ray Absorption Spectroscopy Using IFEFFIT. J Synchrotron Rad. 2005;12:537-41.

[53] Du N, Xu Y, Zhang H, Zhai C, Yang D. Selective Synthesis of Fe_2O_3 and Fe_3O_4 Nanowires Via a Single Precursor: A General Method for Metal Oxide Nanowires. Nanoscale Research Letters. 2010;5(8):1295-300.

[54] Iida H, Takayanagi K, Nakanishi T, Osaka T. Synthesis of Fe_3O_4 Nanoparticles with Various Sizes and Magnetic Properties by Controlled Hydrolysis. Journal of Colloid and Interface Science. 2007;314(1):274-80.

[55] Wang WW, Zhu YJ, Ruan ML. Microwave-assisted Synthesis and Magnetic Property of Magnetite and Hematite Nanoparticles. Journal of Nanoparticle Research. 2007;9(3):419-26.

[56] Linh PH, Thach PV, Tuan NA, Thuan NC, Manh DH, Phuc NX, et al. Magnetic Fluid Based on Fe_3O_4 Nanoparticles: Preparation and Hyperthermia Application. IOP Publishing; p. 012069.

[57] Hyeon T, Lee SS, Park J, Chung Y, Na HB. Synthesis of Highly Crystalline and Monodisperse Maghemite Nanocrystallites without a Size-selection Process. Journal of the American Chemical Society. 2001;123(51):12798-801.

[58] Lu J, Jiao X, Chen D, Li W. Solvothermal Synthesis and Characterization of Fe_3O_4 and γ-Fe_2O_3 Nanoplates. The Journal of Physical Chemistry C.

2009;113(10):4012-7.

[59] Mills P, Sullivan J. A Study of the Core Level Electrons in Iron and its Three Oxides by Means of X-ray Photoelectron Spectroscopy. Journal of Physics D: Applied Physics. 1983;16:723.

[60] Yamashita T, Hayes P. Analysis of XPS Spectra of Fe^{2+} and Fe^{3+} Ions in Oxide Materials. Applied Surface Science. 2008;254(8):2441-9.

[61] Batlle X, Labarta A. Finite-size Effects in Fine Particles: Magnetic and Transport Properties. Journal of Physics D: Applied Physics. 2002;35:R15.

[62] Morel AL, Nikitenko SI, Gionnet K, Wattiaux A, Lai-Kee-Him J, Labrugere C, et al. Sonochemical Approach to the Synthesis of Fe_3O_4@ SiO_2 Core− Shell Nanoparticles with Tunable Properties. Acs Nano. 2008;2(5):847-56.

[63] Williams AGB, Scherer MM. Spectroscopic Evidence for Fe (II)-Fe (III) Electron Transfer at the Iron Oxide-water Interface. Environmental Science & Technology. 2004;38(18):4782-90.

[64] Laaksonen T, Santos H, Vihola H, Salonen J, Riikonen J, Heikkilä T, et al. Failure of MTT as a Toxicity Testing Agent for Mesoporous Silicon Microparticles. Chemical Research in Toxicology. 2007;20(12):1913-8.

[65] Hussain S, Hess K, Gearhart J, Geiss K, Schlager J. In Vitro Toxicity of Nanoparticles in BRL 3A Rat Liver Cells. Toxicology in Vitro. 2005;19(7):975-83.

[66] Holman HYN, Goth-Goldstein R, Blakely EA, Bjornstad K, Martin MC, McKinney WR. Individual Human Cell Responses to Low Doses of Chemicals Studied by Synchrotron Infrared Spectromicroscopy. Biomedical Spectroscopy: Vibrational Spectroscopy and Other Novel Techniques 2000, p. 57-63.

[67] Abdel-Raouf Ahmed G, Khorshid FAR, Kumosani TA. FT-IR Spectroscopy as a

Tool for Identification of Apoptosis-induced Structural Changes in A549 Cells Treated with PM 701. International Journal of Nano and Biomaterials. 2009;2(1):396-408.

[68] Blankenberg FG, Storrs RW, Naumovski L, Goralski T, Spielman D. Detection of Apoptotic Cell Death by Proton Nuclear Magnetic Resonance Spectroscopy. Blood. 1996;87(5):1951-6.